Plasma Evolution in Laser Powder Bed Fusion using a Double Pulse Format: Time-resolved Measurements and Physics-based Modeling

Mengchen Wu[#], Weidong Liu[#], Zahid Hussain Shah, Benxin Wu[*] and Hanyu Song

School of Mechanical Engineering, Purdue University, West Lafayette IN, USA

Abstract: A novel laser powder bed fusion (LPBF) process utilizing a special double-pulse format was previously proposed. In this process, typically two different types of laser pulses are fired alternatively in time: the low-intensity "sintering laser pulses" intended to melt and coalesce particles, followed by the high-intensity "pressing laser pulse(s)" intended to induce plasma to generate high pressure onto the powder bed to suppress balling and enhance the density of the sintered material. Laser-induced plasma plays a key role in the novel double-pulse LPBF process, but has not been studied sufficiently. Some critical questions remain to be better answered, such as: what is the minimum plasma-induced pressure needed to effectively suppress balling and how do the "sintering pulses" influence the plasma evolution? This paper reports a model-experiment integrative study of the plasma in DP-LMS, which is seldom reported in a paper in literature to the authors' knowledge. The plasma evolution is observed in-situ with a high temporal resolution using an intensified CCD (ICCD) camera. The optical emission spectrum (OES) of the plasma is measured and the plasma temperature is deduced from the OES. A physics-based model for the plasma is developed by combining multiple modules. Under the investigated conditions, the model predictions show acceptable agreements with the measured plasma temperature and top front propagation. Utilizing the model, it has been found that under the conditions studied, the minimum plasma-induced pressure required to effectively suppress balling is approximately the pressure making the Weber number exceed ~1 for the approximately analogized process of a droplet impacting a solid surface. The effect of the "sintering pulses" also influences the evolution of the plasma and obviously increase the plasma-induced pressure on the powder bed surface.

Keywords: Laser powder bed fusion; pulsed laser; laser-induced plasma; double pulse

1. Introduction

Additive manufacturing sees many current or potential applications in multiple fields due to its special capability of rapid and flexible part production [1]. In particular, powder-based additive manufacturing processes using a laser beam as the energy source, such as laser powder bed fusion (LPBF), can produce parts with complicated geometries and made of different types of materials [2, 3]. Continuous wave (CW) lasers are frequently utilized in these additive

[*] Corresponding author: Benxin Wu, Professor, School of Mechanical Engineering, Purdue University, 585 Purdue Mall, West Lafayette, IN 47907, USA, email: wu65@purdue.edu. [#]Contribute equally.

manufacturing processes [4, 5]. However, short-pulsed lasers, although less commonly used, can have their special potential advantages, such as relatively high spatial resolutions, large laser power densities that can be achieved and/or good process adjustability [6, 7]. Typically, conventional laser-based additive manufacturing processes use powders with sizes around tens of micrometers or larger [8-10]. Since part features are fabricated via laser-generated coalition of particles, the theoretically achievable minimum feature size can become smaller as the particle size decreases. This implies a potential resolution advantage of using smaller powder sizes. In laser micro sintering (which is a process producing microscale part features via laser-induced particle coalition), small powder sizes of a few micrometers or smaller (< ~10 μm) as well as short-pulsed lasers (e.g., nanosecond-pulsed lasers) are frequently employed [8, 11-13]. In this paper, laser sintering is broadly defined as any process of particle coalition induced by laser beam irradiation regardless of the extent of the particle melting.

Despite the aforementioned potential advantages for employing short-pulsed lasers and fine metal powders (e.g., a few micrometers or smaller) in laser sintering, in such a situation it can often be relatively challenging to achieve good continuity and high densification in the produced part material [8]. A low relative density of the sintered material and/or the detrimental balling phenomenon are often seen [8, 11, 13]. The small powder particles can have high inter-particle forces relative to gravity, leading to easiness of agglomeration [11], and the powder can often have a relatively high pre-sintering porosity [8, 13].

A novel additive manufacturing process named “double-pulse laser micro sintering” (DP-LMS) was proposed by B. Wu and a related patent was granted [14]. DP-LMS utilizes two types of laser pulses: a certain number of “sintering laser pulses” are first shot, which are then followed by one or multiple “pressing laser pulses” shot at a certain moment after the last sintering pulse.

Such a pulse train is called a "pulse group", and will be repeated as the laser spot scans the powder material surface. Typically, the "sintering pulses" are featured by a long duration and low intensity, and are intended to melt powder particles and cause their coalition. The "pressing pulses" have a short pulse duration and high intensity, and are intended to ablate a small amount of powder material and produce plasma. The plasma-induced high transient pressure on the surface of the powder material can promote molten material flow, suppress balling, and/or improve the continuity and density of the sintered material. The use of two different kinds of laser pulses also gives the potential advantage of good flexibility and adjustability in manufacturing. DP-LMS itself does not require or preclude additional pre-sintering mechanical compaction of each powder layer after powder spreading (the additional mechanical compaction step for each layer may help enhance the sintered material density [8], but obviously will also increase the total manufacturing time).

In the authors' previous papers, DP-LMS using very fine cobalt [12, 13] or iron [15] powders have been studied. Under the study conditions in Refs. [12, 13, 15], the DP-LMS process can produce much better material continuity, lower porosity and/or less serious balling than the process using only the sintering pulses. As introduced earlier, laser-induced plasma plays the key role in generating the better results in DP-LMS. Hence, a good understanding of the plasma evolution in DP-LMS is crucial. It is very desirable to conduct a study integrating time-resolved measurements and physics-based modeling to improve the understanding of the plasma. However, such a study for plasma induced from a powder bed using the special laser pulse format in DP-LMS is rare in a paper in literature to the authors' knowledge.

Many studies for laser-induced plasma were reported in literature (e.g., [16-32], However, most reported studies are not for plasma generated by laser interactions with powders or particles.

Refs.[16-21] studied such plasma, but the plasma was not induced with the special laser pulse format in DP-LMS.

In the authors' previous study in [16], time-resolved imaging and physics-based modeling of plasma produced by a single ~4-ns laser pulse from a cobalt powder bed were performed. The model-predicted plasma top front locations in the early stage show a reasonably good agreement with those from the imaging. However, the modeling and experimental study in [16] is not on DP-LMS, which uses both sintering and pressing pulses in each pulse group. Besides, the plasma temperature was not measured in Ref [16]. Ref. [17] reports an experimental study of plasma induced during Cu-based powder sintering by Q-switched pulsed YAG laser. Time-resolved images of the plasma were taken, and the plasma OES were measured, from which the plasma electron densities and temperatures were deduced. No physics-based computational modeling work was conducted in [17]. Ref. [18] investigated nanosecond-pulsed laser interactions with metallic particles on a transparent plate, including the plasma plume induced, where time-resolved shadowgraph imaging was conducted in the experimental work. Ref. [19] investigated the optical emission from plasma produced by nanosecond-pulsed laser ablation of copper micro particles with a diameter of 49-390 μm, and discovered a steplike behavior, i.e., the plasma emission intensity has a sudden jump as the particle diameter increases above a certain value. Ref. [20] reports an experimental and modeling study for CW laser-based powder bed fusion, involving laser-induced plasma plume. Ref. [21] studied the monitoring of a selective laser melting process (using a CW laser) through the OES measurement of the laser-induced plume, and found a correlation between the OES and the melt pool size.

None of the studies introduced in the previous paragraph is for the DP-LMS process. DP-LMS utilizes a very special laser pulse format, typically involving both long, low-intensity

sintering pulses and short, high-intensity pressing pulse(s) in each laser pulse group. Due to the crucial role of plasma in DP-LMS, a further study on the plasma is clearly needed. In particular, the following critical questions remain to be better answered: (1) How do the "sintering pulses" influence the plasma generated by the pressing pulse in each pulse group? (2) What is the minimum plasma-induced pressure needed to effectively suppress balling for good densification of sintered material? These questions were not answered in the authors' previous paper [16]. Ref. [16] studied plasma generated by a single nanosecond (ns) laser pulse instead of the "laser pulse group" with the special pulse format in DP-LMS, and thus did not answer Question (1). In addition, Ref. [16] did not answer the critical Question (2), either.

In this paper, an experiment-model integrative study is performed for the plasma induced during DP-LMS. On the experimental side, time-resolved imaging of the plasma evolution is conducted using an ICCD camera with a resolution of ~3 ns. The plasma OES is measured and the plasma temperature is then deduced based on the OES (plasma OES measurements were not performed in the authors' previous paper [16]). On the modeling side, a physics-based model for DP-LMS is developed based on the authors' previous work [7, 16]. The model is validated by comparing its predictions with the experimentally measured plasma top front propagation and temperature. Then the model is employed to improve the understanding of the plasma in DP-LMS and answer the two critical questions listed in the previous paragraph. To avoid making this paper excessively long, some related information or details are given in the "Supplemental Material" file for this paper.

2. Experiments

Three types of time-resolved measurements or observations have been performed during DP-LMS: (1) Time-resolved imaging for plasma during DP-LMS using an ICCD camera with a ~3-ns gate width; (2) Plasma OES measurement using a spectrometer to deduce the plasma temperature; and (3) Imaging of the laser-irradiated region on the surface of the powder bed using a camera with an exposure time of ~41 μs.

This study utilized the cobalt powder from Alfa Aesar (Product No.: 10455), with a ~1.6-μm nominal particle size according to the powder's product specification. First, the powder was placed into ~95% ethanol and dispersed ultrasonically for approximately two minutes to reduce particle agglomeration. Then the powder in ethanol was stirred by a magnetic stirrer for around two minutes. After this, the above ultrasonic dispersion and magnetic stirring processes were repeated twice. Then the cobalt powder was spread into the powder bed using a doctor blade. After the powder dried naturally, the experiments of laser sintering were performed. The total thickness of the particle layer in the powder bed is around ~220 μm. Based on the cobalt bulk density [33], the powder weight measured and the apparent powder volume in the powder bed, the powder pre-sintering porosity is estimated to be around 69%.

2.1 Time-resolved Imaging of Plasma Plume via ICCD Camera

Figure 1a gives the schematic diagram for the DP-LMS experimental setup (similar to the setup in the authors' previous paper [13]), together with the plasma time-resolved imaging apparatus. In the DP-LMS experiments in this paper, as shown in Fig.1c, 10 "sintering laser pulses" are fired with a 40-μs pulse-to-pulse time interval. Then 1 "pressing laser pulse" is delivered to the powder bed with a temporal distance of ~5 μs from the 10^{th} "sintering pulse". The "10+1" pulse format is not necessarily the only possible good choice in DP-LMS. It is utilized because a similar

pulse format has produced reasonably good sintering results in the author's previous studies [13, 15].

The 10 sintering pulses (coming from a SPI G3 laser; wavelength: ~1064 nm) have a long full duration of ~200 ns/pulse and a low pulse energy of ~0.031 mJ/pulse, and their intended purpose is to melt the particles in the surface area irradiated. On the other hand, the pressing pulse (from a Bright Solutions ONDA laser; wavelength: ~1064 nm) has a much shorter full-width-at-half-maximum (FWHM) duration equal to ~4 ns and a higher pulse energy of ~0.120 mJ (unless indicated otherwise), leading to a much higher transient laser intensity. It is intended to produce a plasma plume to generate a high pressure pulse on the powder bed, promoting molten material flow, and suppressing baling and/or improving material continuity and densification after solidification. The control of the relative timing of the pressing and sintering pulses is achieved via the digital delay generator. The diameters of the spots for the sintering and pressing laser pulses on the powder bed surface are ~82 μm and ~157 μm, respectively. They are approximately measured using the knife-edge method under the assumption that both beams follow Gaussian intensity profiles. The two beams are aligned in a way such that they have approximately the same central axis after they pass the beam splitter. It should also be noted that the simulation results given in this paper are for the laser parameters described in this paragraph and illustrated in Fig.1c, unless indicated otherwise.

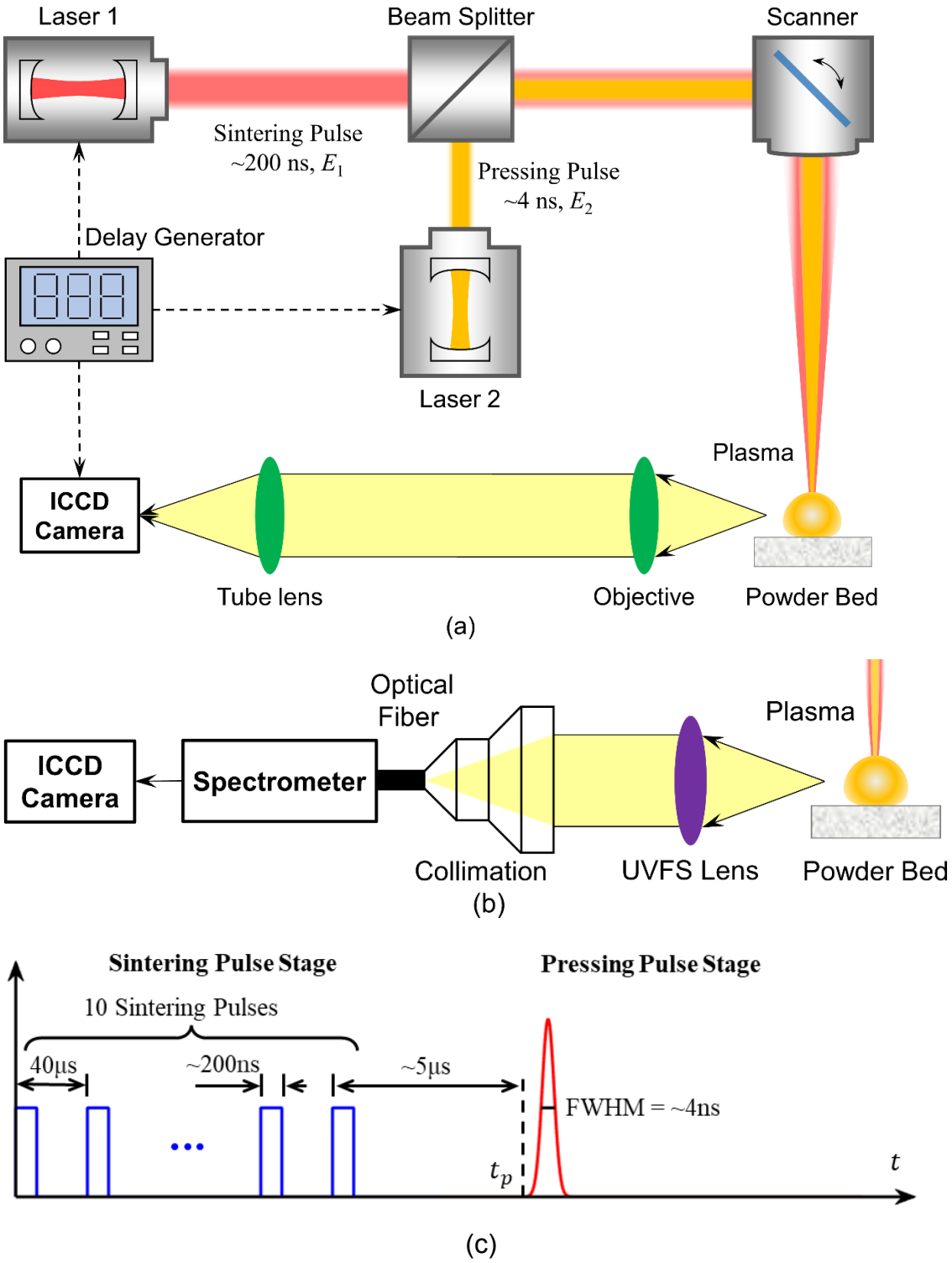

Figure 1. The schematic diagram showing the major components of the experimental system for DP-LMS together with the time-resolved plasma imaging setup (a); the schematic showing the plasma OES setup (b); and the sequence of sintering pulses and pressing pulse in a pulse group during DP-LMS (t_p: pressing pulse arrival moment) (c). The plot in (c) does not necessarily show the actual shapes or intensities of the pulses.

The time-resolved imaging system mainly consists of an objective lens (f = 20 mm), a tube lens (f = 200 mm) and an ICCD camera (Andor, DH 334T-18U-E3). The objective and tube lens lead to a 10X magnification. According to the product specification, the ICCD detector has a pixel size of ~13 μm × ~13 μm. Thus, in an ICCD image each pixel corresponds to an actual physical domain size of ~1.3 μm × ~1.3 μm. The ICCD gate width is chosen as ~3 ns in the plasma imaging experiments, while the gain is set as 1000. The moment of ICCD gate opening (i.e., the moment of image capturing) relative to the beginning of the pressing laser pulse is controlled via the delay generator. One image is captured in each experiment and then the laser spot is moved to a fresh powder bed surface location to take the next image. From the images captured at different delay times, the temporal evolution of the plasma size and shape can be obtained. For the ICCD images given in this paper, the time labeled refers to the moment of the ICCD gate closing.

2.2 OES Measurement and the Deduction of Plasma Temperature

Figure 1b shows the experimental setup for the time-resolved OES measurement. In the OES measurement system, the Thorlabs uncoated UV-Grade Fused Silica (UVFS) lens (f = 50 mm) and collimation package (f = 33.9 mm) collects optical emission from the plasma plume into an optical fiber bundle (Thorlabs, BF20HSMA01, core diameter: ~550 μm). The fiber delivers the emission into a spectrometer (Andor, SR-500i-A) that spatially separates light at different wavelengths with a 1200 l/mm grating. An ICCD camera is attached to the spectrometer as the detector to measure and obtain the spectrum of the light emitted from the plasma. The OES measurement temporal resolution is determined by the gate width of the ICCD camera, chosen as ~40 ns for the OES result given in this paper. The ICCD gain is set as 3000 for the OES measurement. Prior to measurements, the spectrometer went through a calibration process. The

wavelength calibration was achieved using a mercury-argon wavelength calibration source from Ocean Insight (HG-2). To enhance the signal-to-noise ratio (SNR) in the spectrum, each OES used for plasma temperature deduction was obtained by accumulating signals from twenty measurements performed under the same DP-LMS condition. Prior to the plasma OES measurements, the background signals (due to noises, etc.) were acquired and then subtracted from the plasma OES measured.

The plasma temperature can be deduced from the measured OES. If the plasma plume can be assumed to be optically thin and in local thermodynamic equilibrium [34-39], then the measured spectral line intensity resulted from the transition between an upper energy level *m* and a lower energy level *n* of a certain plasma species (e.g., neutral cobalt atoms), I_{mn}, can be related to the plasma species excitation temperature *T* via the following relation [34, 35]:

$$ln\left(\frac{I_{mn}\lambda_{mn}}{g_m A_{mn}}\right) = -\frac{1}{k_b T}E_m + ln\left[\frac{FhcN_s}{U_s}\right] \qquad (1)$$

where k_b, c and h represent the Boltzmann constant, vacuum speed of light and Planck constant, respectively, A_{mn} denotes the transition probability, λ_{mn} denotes the wavelength, g_m and E_m denote the upper level's statistical weight and energy, respectively, N_s and U_s are the species' total number density and partition function, respectively, and F is a parameter related to the plasma volume and the collection efficiency of the optical emission measurement system [35]. From the measured plasma OES, the spectral line intensities for the transitions of multiple upper-lower energy level pairs for the same type of species can be obtained. Then multiple points can be obtained in the plot for $\ln(\frac{I_{mn}\lambda_{mn}}{g_m A_{mn}})$ versus E_m. The multiple points can be fitted by a straight line, whose slope is approximately $-\frac{1}{k_b T}$. From the slope, the plasma temperature *T* can be obtained. In this study, the measured OES data for a spectral line peak is first fitted by the Voigt function [40-

42] using the LMFIT Python package [43] based on the least-square method. Then the spectral line integral intensity I_{mn} can be obtained.

2.3 In-situ Imaging of Powder Bed Surface

The powder bed surface was observed in situ using a camera during DP-LMS as shown in Fig.2. The objective and tube lens used together with the camera (PixeLINK PL-D755MU-T) are the same as those used in the ICCD imaging setup in Fig.1a. The exposure time of the camera is set as ~41 μs for the results shown in this paper. The image capturing is triggered by a digital delay generator to start at ~6.3 μs after the pressing laser pulse in DP-LMS (or after the last sintering pulse in SP-LMS that uses only the sintering pulses). During DP-LMS, the hot area of the powder bed surface (e.g., the melt pool) emits relatively intense light and hence can show up as a bright region in the image. The images can reveal useful information about the DP-LMS and the SP-LMS processes, which will be discussed in detail later.

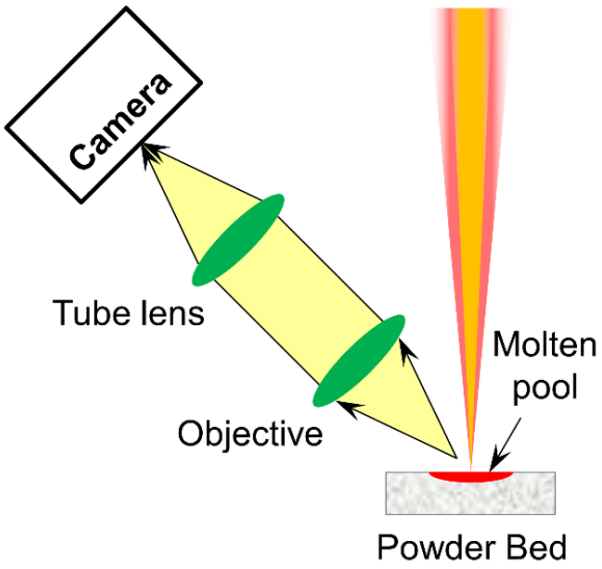

Figure 2: Schematic of the optical apparatus for time-resolved imaging of the power bed surface in DP-LMS

3. Model for Plasma Generation and Evolution in DP-LMS

In the studied DP-LMS process, 10 sintering laser pulses are followed by 1 pressing laser pulse fired at ~5 μs after the 10^{th} sintering pulse in each pulse group. The sintering pulses have a relatively low intensity and a long pulse duration (~200 ns) with a 40-μs pulse-to-pulse time interval. They do not generate a plasma plume under the condition studied. However, they will generate a surface melt pool in the powder bed that is still in existence when the pressing laser pulse arrives (as found from the model simulation in this study). In addition, the air condition (temperature, density and pressure) near the laser spot on the powder bed surface will be altered by the powder-air heat transfer during the irradiation of the 10 sintering pulses. Different from the sintering laser pulses, the pressing laser pulse has a much shorter pulse duration (~ 4 ns) and a much higher peak intensity. It drives the melt pool surface temperature to a very high value, causing significant surface vaporization and plasma formation. The generation and evolution of the plasma may be affected by the powder bed temperature and the ambient air condition at the moment of the pressing pulse's arrival, which are influenced by the preceding sintering pulses.

The authors' prior paper [7] reported the thermal modeling of the temperature field in a micro metallic powder bed induced by low-intensity ~200-ns laser pulses. In the authors' another previous paper [16], the plasma plume produced by a single ~4-ns laser pulse irradiation of a micro metallic powder bed was simulated using a thermal and gas dynamic model. However, neither [7] nor [16] modeled the plasma plume generation and evolution during DP-LMS.

Based on the authors' previous work in [7] and [16], this paper reports the modeling of the plasma generation and evolution in DP-LMS. The modeling or measurement of the plasma evolution in DP-LMS is seldom in a paper in literature to the authors' knowledge. The modeling and measurement results in this paper provide new knowledge on plasma properties and evolution

in DP-LMS. This study will answer the following previously unanswered questions: (1) How do the "sintering pulses" influence the plasma generated by the "pressing pulse" in DP-LMS? (2) What is the minimum plasma-induced pressure needed to effectively suppress balling for good densification of sintered material? Thus, this work has a clear novel contribution to the field.

The powder particle has a small nominal size, which is only ~1.6 μm. Hence, a model explicitly tracking and simulating the evolution of all particles would be too expensive (if feasible at all) computationally. Hence, in this model an approximate assumption has been made that the powder bed is a continuum medium with effective material properties depending on its porosity. In addition, under the conditions studied the plasma is produced due to rapid evaporation (on the scale of nanoseconds) from the powder bed surface. It is assumed that the effect of the molten material flow in the condensed phase on the plasma evolution can be approximately neglected. These assumptions have greatly reduced the computational cost of the model. The model-predicted plasma front propagation and temperature will be compared with experimental measurements to verify if the model can still have an acceptable accuracy with these simplified assumptions. In the plasma measurements in this paper (the imaging as well as the optical emission spectroscopy (OES) measurements to obtain plasma temperature), only one laser pulse group is sent and the laser spot does not move during each measurement. Hence, it is sufficient to develop a 2D axisymmetric model to compare its simulation results with the measurement results.

3.1 Overall Structure of the Model

Figure 3 illustrates the model's overall structure. The simulated process can be divided into two stages: the sintering pulse stage from t = 0 to 365 μs and the pressing pulse stage after the pressing laser pulse arrives at t = 365 μs. The model has three modules: (1) the "Powder Bed

Module in the Sintering Pulse Stage", which simulates the temperature evolution in the powder bed during the irradiation of the 10 sintering pulses in the pulse group (from $t = 0$ to 365 μs); (2) the "Air Module in the Sintering Pulse Stage", which simulates the evolution of the ambient air as well as the air in the pores of the powder bed due to the powder-air heat transfer during the irradiation of the 10 sintering pulses (from $t = 0$ to 365 μs); and (3) the "Pressing Pulse Stage Module" (for $t > 365$ μs), which simulates the pressing laser pulse-induced plasma evolution by solving governing equations in the gaseous phase as well as the powder bed regions.

The computational domain for Module (1) is a region in the powder bed around the laser spot. The domain for Module (2) includes both the domain of Module (1) in the powder bed (which has air in the pores of the powder bed) and a region above the powder bed. First, the simulation with Module (1) is performed. The predicted temperature history in the powder bed is loaded into Module (2) (for the portion of its domain in the powder bed), based on which the simulation with Module (2) is conducted. The simulation results from Module (1) and (2) at $t = 365$ μs (right before the arrival of the pressing pulse) are loaded into Module (3) as its initial conditions. Then the simulation with Module (3) is performed.

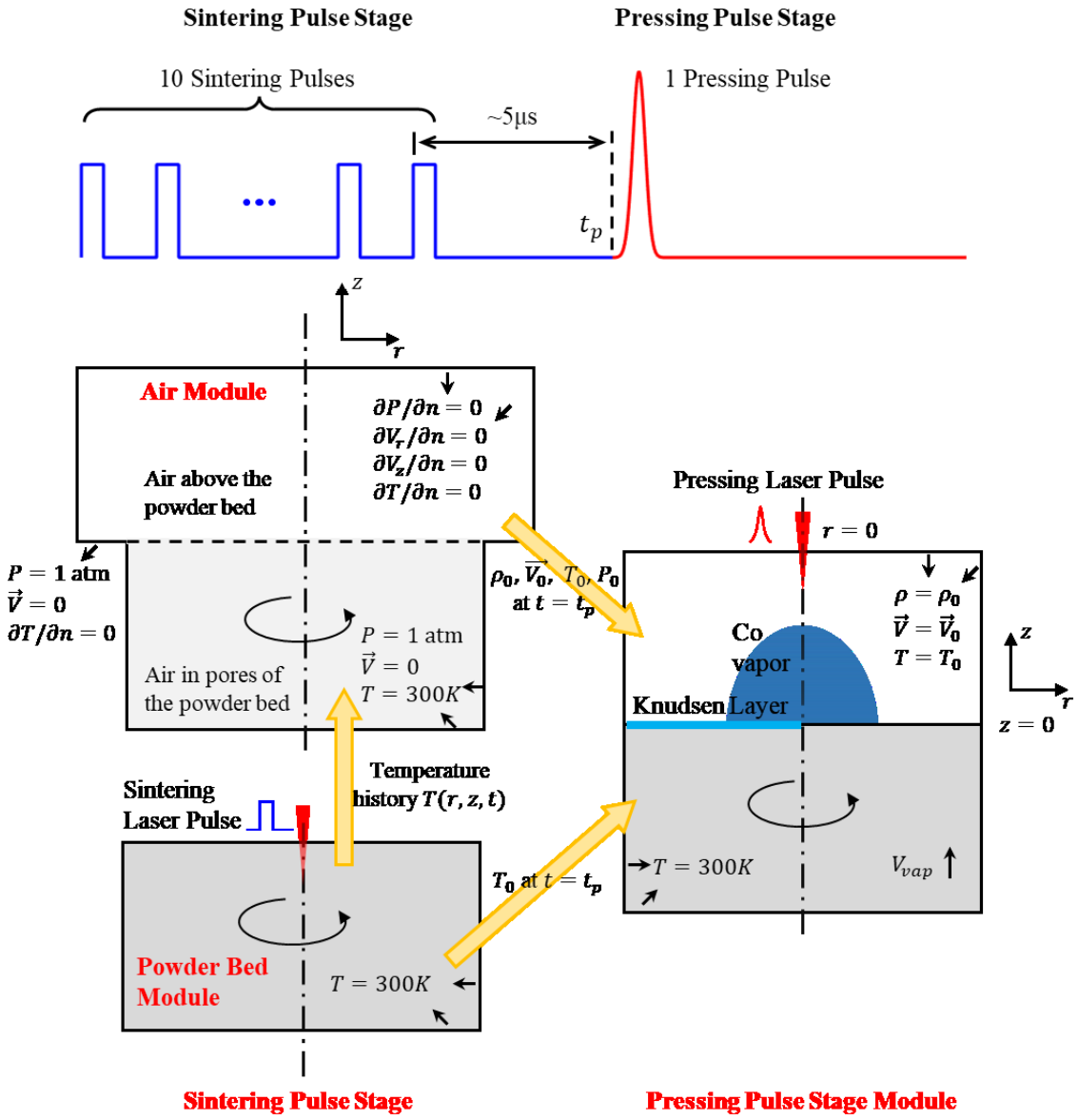

Figure 3. Schematic of the structure and setup of the model for plasma generation and evolution in DP-LMS (ρ_0, $\overrightarrow{V_0}$, T_0 and P_0 are the density, velocity, temperature and pressure spatial distributions at $t = t_p$ predicted by the sintering pulse stage modules. $\partial/\partial n$ is the spatial derivative in the normal direction of a boundary).

3.2 The Powder Bed Module in the Sintering Pulse Stage

This module simulates the evolution of the temperature field of the powder bed induced by the 10 sintering pulses by solving the following heat transfer equation [7, 44, 45]:

$$\frac{\partial \rho H}{\partial t} = \frac{1}{r}\left[r k_{eff} \frac{\partial^2 T}{\partial r^2} + \frac{\partial T}{\partial r}\frac{\partial}{\partial r}(k_{eff} r)\right] + \frac{\partial}{\partial z}\left(k_{eff}\frac{\partial T}{\partial z}\right) + \frac{\partial I(r,z,t)}{\partial z} \qquad (2)$$

where t represents time, r and z denote spatial coordinates in the r and z direction, respectively, H denotes the powder material (cobalt) enthalpy per unit mass, which is related to T (temperature) through the bulk cobalt specific heat as well as the latent heat of melting (for temperatures reaching or exceeding the melting starting point), and ρ is the effective density of the powder bed medium, which is related to the bulk cobalt's density ρ_{co} and the powder bed's porosity φ by: $\rho = \rho_{co}(1-\varphi)$, where the density of air filling the pores is very small and hence has been neglected.

When the powder bed medium is in the solid phase, its effective thermal conductivity k_{eff} is roughly assumed to be 3% of the bulk cobalt conductivity k_{co}, where the percentage value is estimated based on the information from the computational study of metal powder conductivities in Ref. [46] for iron powder considering the similarity of regular properties between iron and cobalt [33, 46-48]. When the medium is in the molten state (or re-solidified after melting), it is assumed $k_{eff} = k_{co}(1-\varphi) + k_{air}\varphi$ [49], where k_{air} is the air thermal conductivity. In the last term on Eq. (2)'s right side, $I(r,z,t)$ represents the laser intensity. Its variation with z inside the powder bed (which corresponds to the absorption of laser energy) is calculated using the analytical model from [50] based on the particle size and powder porosity. If melting occurs at the powder bed surface, then the surface evaporation flux is calculated based on the surface temperature using the Hertz-Knudsen equation with a constant vaporization coefficient of ~0.82 and a saturation vapor pressure determined from the Clausius-Clapeyron equation [7, 44, 51-53].

Eq. (2) was solved using a computer code established by the authors' team [7] utilizing an explicit finite difference method [54] based on MATLAB (version R2020b. The MathWorks, Inc.). Some additional information about this module is given in the "Supplemental Material" file for this paper. This module is based on the thermal model in the authors' prior paper [7], in which more details (when not given in any file for this paper) are available.

3.3 The Air Module in the Sintering Pulse Stage

Due to the irradiation of the 10 sintering pulses, the powder's temperature is elevated, causing the powder-air heat transfer. Air exists in both the pores of the powder bed and the region above the powder bed surface. The powder-air volumetric heat capacity ratio is very large. Thus, the powder-air heat transfer is expected to have a small overall effect on the powder's temperature field and hence is neglected in the calculation in the "Powder Bed Module in the Sintering Pulse Stage". However, since air has a much smaller heat capacity per unit volume than the powder, the powder-air heat transfer may significantly change the temperature and density of the air in the pores of the heated powder bed region and the ambient air above the laser-irradiated surface region of the powder bed. This may influence the subsequent evolution of plasma induced by the pressing laser pulse. Hence, the "Air Module in the Sintering Pulse Stage" is to simulate the gas dynamic process of the air in the pores of the powder bed and in the region above the surface of the powder bed due to the heat transfer from the powder in the sintering pulse stage.

A schematic for the domain of this module is included in Fig.3, which also shows the domain boundary conditions. The evolution of the air is simulated using OpenFOAM [55-58] to solve 3D compressible gas dynamic equations on a wedge of 5°, where the wedge boundary

condition [59] is used in the azimuthal direction, leading to an approximately equivalent 2D axisymmetric description of the air evolution.

For the air module's computational domain above the powder bed's surface, the governing equations include the continuity, momentum and energy equations for compressible gas. Gravity and viscous stresses are considered in the governing equations, but turbulence is not. For the air module's computational domain in the powder bed, air flows in the pores. What needs to be modeled is a fluid flow process in a porous medium [60-66]. The ideal gas equation of state (EOS) is used for air, while the air viscosity and thermal conductivity as a function of the air temperature and density are taken from Ref. [67]. The air specific heat C_p is assumed to be constant and equal to 1004 J/kg·K [68-70].

It is assumed that the temperature history of the air at a spatial point in the powder bed is the same as that for the powder at the same spatial point, which is taken from the simulation result of the "Powder Bed Module in the Sintering Pulse Stage". Hence, there is no need to solve the energy equation for the air in the powder bed domain. The continuity and momentum equations for the compressible air in the porous medium of the powder bed are given as [60-66, 70]:

$$\frac{\partial(\varepsilon_p \rho)}{\partial t} + \nabla \cdot (\rho \vec{u}) = 0 \tag{3a}$$

$$\frac{\partial(\rho \vec{u})}{\partial t} + \nabla \cdot (\rho \vec{u} \vec{v}) = -\varepsilon_p \nabla \mathrm{P} + \nabla \cdot (\tilde{\tau}) + \vec{F}_d + \varepsilon_p \rho \vec{g} \tag{3b}$$

where ρ and P denote the air density and pressure, respectively, ε_p is the medium porosity, $\vec{u}$ is the air Darcy velocity in the porous medium ($\vec{u} = \varepsilon_p \vec{v}$, where $\vec{v}$ is the air interstitial velocity), $\tilde{\tau}$ is the viscous stress tensor calculated based on $\vec{u}$, $\vec{g}$ is the gravitational acceleration vector, and $\overrightarrow{F_d}$ is the volumetric force on the air due to the powder particles.

At t = 0, the air is assumed to have zero velocity, a pressure of 1 atm and a temperature of 300 K. Some further details about the Air Module are given in the "Supplement Material" file for this paper.

3.4 The Pressing Pulse Stage Module

The Pressing Pulse Stage Module is to simulate the generation and evolution of the plasma induced by the pressing pulse. As shown in Fig.3, the computational domain of this module includes both the powder bed region and the ambient gaseous phase region, where the heat transfer equation and the gas dynamic equation are solved, respectively. The calculation with this module starts at t = 365 μs (when the pressing laser pulse starts). The simulation results at t = 365 μs from the "Powder Bed Module in the Sintering Pulse Stage" and the "Air Module in the Sintering Pulse Stage" will be used as the initial conditions of the powder bed region and the ambient gas region, respectively, for the "Pressing Pulse Stage Module".

When surface evaporation occurs, the powder bed surface recedes at a velocity of V_{vap} (called "surface evaporation velocity"). The z coordinate system is defined in a way such that z = 0 is always positioned at the top surface of the powder bed. In such a coordinate system, the condensed phase material of the powder bed moves in the +z direction at V_{vap} as shown in Fig.3. Thus, in this module the heat transfer equation in the powder bed region is similar to Eq. (2), except that an additional term, $V_{vap}\frac{\partial \rho H}{\partial z}$, is added on the left side of the equation.

In the "Pressing Pulse Stage Module", as introduced in the authors' prior paper [16], the powder bed surface reflectivity for the laser beam is determined using Fresnel equations based upon the material complex refractive index, while the optical absorption coefficient is determined based on the refractive index's imaginary part [71].

The evolution of the material vaporized from the powder surface as well as the ambient air is governed by the two-dimensional compressible gas dynamic equations [16, 44, 72-74]:

$$\frac{\partial \rho_{vap}}{\partial t} + \frac{\partial (\rho_{vap} V_r)}{\partial r} + \frac{1}{r}(\rho_{vap} V_r) + \frac{\partial (\rho_{vap} V_z)}{\partial z} = 0 \tag{4a}$$

$$\frac{\partial \rho_{air}}{\partial t} + \frac{\partial (\rho_{air} V_r)}{\partial r} + \frac{1}{r}(\rho_{air} V_r) + \frac{\partial (\rho_{air} V_z)}{\partial z} = 0 \tag{4b}$$

$$\frac{\partial \rho V_r}{\partial t} + \frac{\partial \rho V_r^2}{\partial r} + \frac{1}{r}(\rho V_r^2) + \frac{\partial (\rho V_r V_z)}{\partial z} = -\frac{\partial P}{\partial r} \tag{4c}$$

$$\frac{\partial \rho V_z}{\partial t} + \frac{\partial \rho V_r V_z}{\partial r} + \frac{1}{r}(\rho V_r V_z) + \frac{\partial (\rho V_z^2)}{\partial z} = -\frac{\partial P}{\partial z} \tag{4d}$$

$$\frac{\partial (0.5\rho V^2 + E_i)}{\partial t} + \frac{\partial [(0.5\rho V^2 + E_i + P) V_r]}{\partial r} + \frac{1}{r}\left(\frac{1}{2}\rho V^2 + E_i + P\right) V_r + \frac{\partial [(0.5\rho V^2 + E_i + P) V_z]}{\partial z} =$$
$$\frac{\partial}{\partial z}\left(k_g \frac{\partial T}{\partial z}\right) + \frac{1}{r}\frac{\partial}{\partial r}\left(r k_g \frac{\partial T}{\partial r}\right) + \alpha I(r, z, t) \tag{4e}$$

where ρ_{vap} and ρ_{air} are the cobalt vapor and air density, respectively, ρ is the total density ($\rho = \rho_{vap} + \rho_{air}$), V_r and V_z represent the r- and z-direction velocity, respectively, V denotes the total velocity magnitude, E_i is the internal energy per unit volume, P is pressure, α is the laser optical absorption coefficient of the gaseous phase, and k_g denotes the gaseous phase thermal conductivity.

Introductions about the cobalt vapor's equation of state (EOS) [69, 75], laser absorption coefficient [76] and thermal conductivity [77] are given in the "Supplement Material" file for this paper. Under the condition studied, in the pressing pulse stage typically the high-temperature air region (with temperatures higher than 2000 K, approximately at which air molecule dissociation begins under a moderate pressure [78]) is very thin (typically < ~10 μm). Besides, nitrogen and oxygen have high ionization potentials [79, 80]. Thus, as a reasonable approximation, in this

module the air dissociation, ionization and absorption of laser beam are not considered [16]. It is also expected that the effect of the air thermal conductivity in this module is small, and thus as an approximation the air thermal conductivity under the regular room condition determined based on [67] has been used.

The boundary condition for the gas dynamic equations at $z = 0$ is based on the Knudsen layer relation [44, 51, 52, 72, 81-84], relating the temperature of the powder bed surface with the vapor state right above the surface. Ref. [44] has listed the Knudsen layer relation. The governing equations in the condensed and gaseous phases are numerically solved together in each time step, using an in-house developed computer code. The gas dynamic equations are solved with an explicit essentially non-oscillatory (ENO) method [85], while the heat transfer equation for the powder bed region is solved with an explicit finite difference method. The "Pressing Pulse Stage Module" is based on the model reported in the authors' prior paper [16], in which more details (when not given in any file for this paper) are available. As introduced earlier, the powder bed medium effective properties are calculated based on the powder bed porosity and the bulk cobalt properties taken from the literature [33, 86-92]. A table summarizing the major bulk cobalt properties used is given in the authors' previous paper [16]. Some additional information is given in the "Supplemental Material" file.

4. Results and Discussions

4.1 Plasma Imaging and OES Measurement Results

Figure 4 (the left column) shows the ICCD imaging results for plasma induced in DP-LMS. The images are taken at different time after the pressing laser pulse arrives. In Figure 4, the moment at which the pressing laser pulse arrives is defined as $t = 0$. The laser beam propagation direction

is downwards and the powder bed surface is located at around the bottom of each image. It can be seen from the figure that the plasma front propagates upwards quickly in the time range given. One interesting phenomenon shown by the images is that after t = ~30 ns, the plume appears to be separated from the powder bed surface and its bottom region is relatively dark, implying a relatively low temperature and/or density.

Figure 5 shows one measured optical emission spectrum (OES) of plasma in DP-LMS in the given wavelength range. The ICCD gate is open from t = ~35 ns to ~75 ns (where t = 0 is defined as the arrival moment of the pressing laser pulse). The spectrum is obtained by accumulating the results from 20 measurements under the same condition. The spectral lines labeled are identified based on (and the labeled values come from) the NIST database [93]. Based on measured OES data, a typical Boltzmann plot constructed is shown in Fig.6. The six spectral lines of neutral cobalt atoms at 356.94 nm, 357.54 nm, 358.72 nm, 384.55 nm, 389.41 nm and 412.13 nm are utilized, leading to six points in the Boltzmann plot. The spectroscopic data used in constructing the plot is listed in Table 1 [93]. Figure 6 shows that the six points can be fitted well by a straight line with R^2 = 0.95. Four Boltzmann plots have been constructed based on four OES results measured under the same condition (where each OES result is the accumulation of the signals from 20 measurements). The plasma temperature has been deduced to be ~ 4820 ± 234 K, where 234 K is the standard deviation of the four temperatures deduced from the four Boltzmann plots.

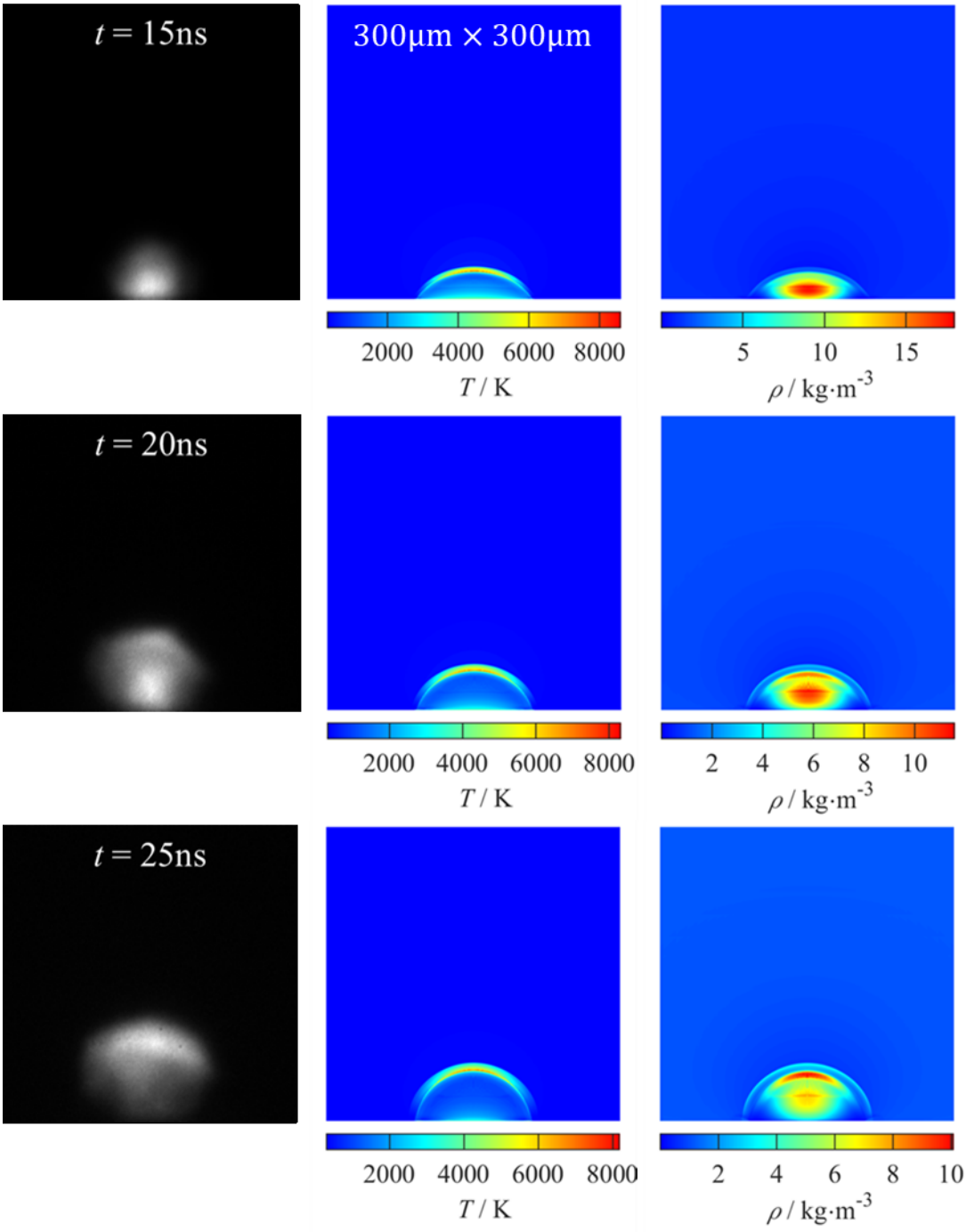

(Figure 4 continues on the next page)

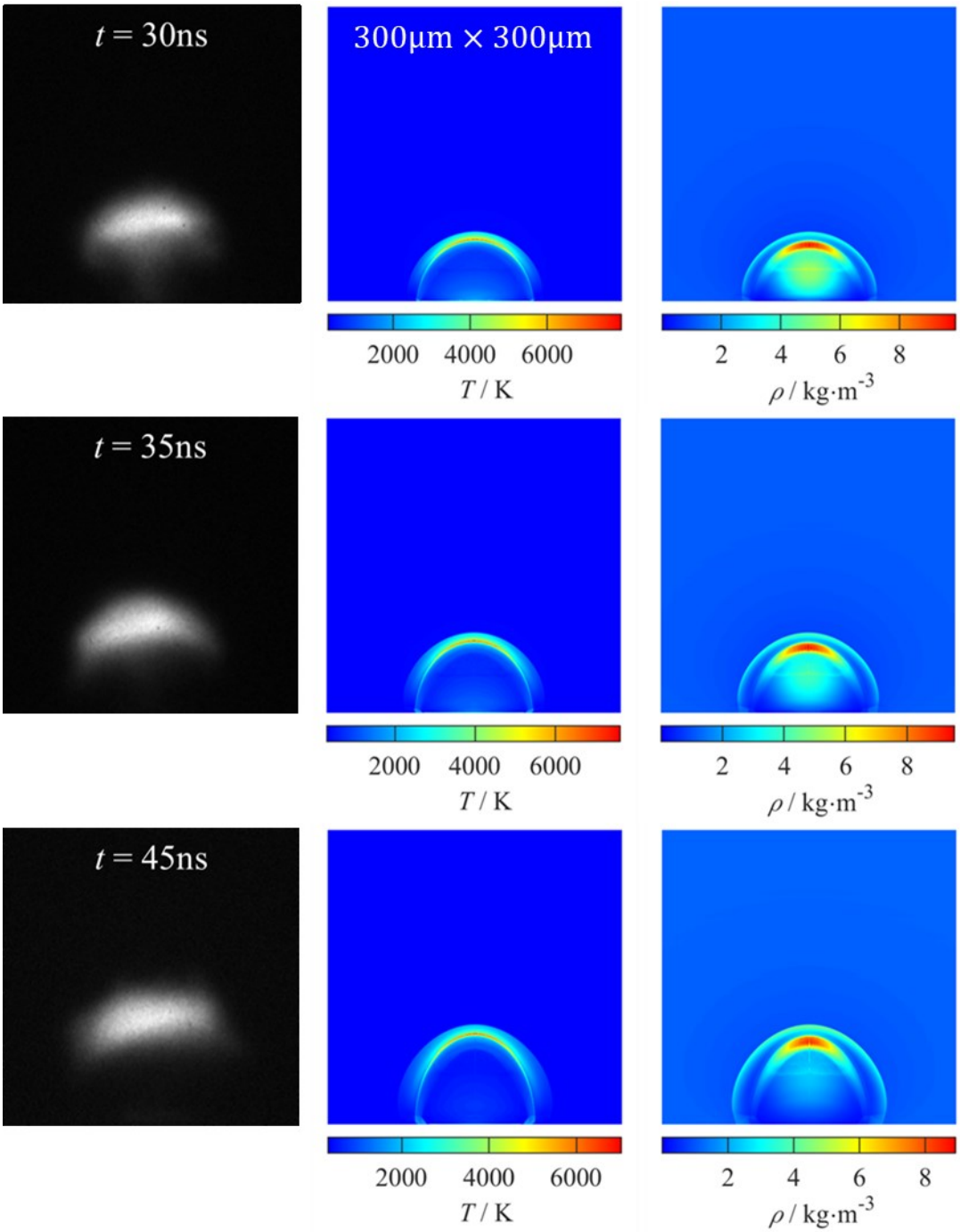

Figure 4. The ICCD images of plasma plume taken at different time after the arrival of the pressing pulse during DP-LMS (left column), compared with the model-calculated gaseous phase material temperature (middle column) and density (right column). The actual physical domain size for each ICCD image or simulation result plot is 300 μm × 300 μm, and the powder bed surface is located at around the bottom. For this figure, t = 0 is defined as the arrival moment of the pressing laser pulse. Each image on the left column is the accumulation of five ICCD images taken under the same condition. In the contour plots, the colors at the plot bottom are based on the model-calculated values at the first row of numerical grid points above the powder bed-gas phase interface (this is also the case for Fig.14 shown later).

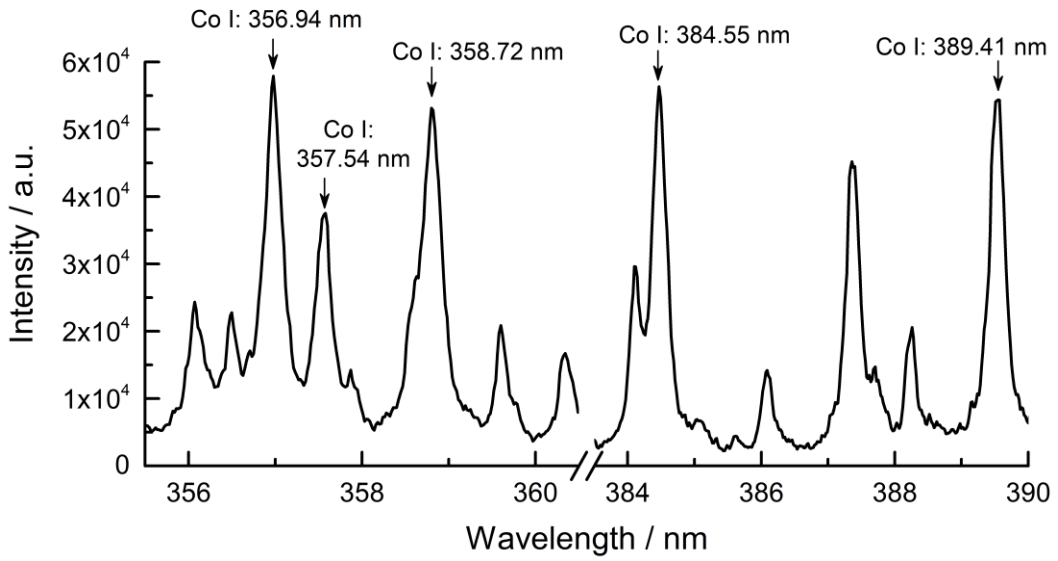

Figure 5. Measured OES of plasma induced during DP-LMS (the ICCD gate is opened from t = 35 ns to 75 ns, where t = 0 is defined as the arrival moment of the pressing laser pulse). (The spectrum is obtained by accumulating 20 measurements under the same condition).

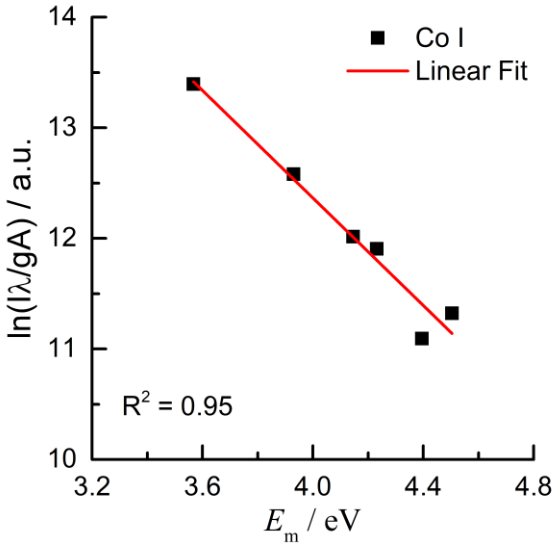

Figure 6. The Boltzmann plot constructed based on the measured plasma OES during DP-LMS (the ICCD gate is opened from t = 35 ns to 75 ns, where t = 0 is defined as the arrival moment of the pressing laser pulse.)

Table 1. Spectroscopic data of Co I lines employed in constructing the Boltzmann plot to deduce the plasma excitation temperature [93].

Wavelength λ (nm)	The upper level's statistical weight g_m	Probability of transition A_{mn} ($\times 10^7$ 1/s)	The upper level's energy E_m (1/cm)
356.94	8	15.00	35450.56
357.54	8	0.96	28777.27
358.72	6	14.00	36329.86
384.55	10	4.60	33439.72
389.41	8	6.90	34133.59
412.13	10	1.90	31699.69

The deduction of plasma temperature with the Boltzmann plot method is based upon the assumption of local thermodynamic equilibrium (LTE), requiring the satisfaction of the McWhirter's criterion [34, 37, 38]. Related discussions are given in the "Supplemental Material" file of this paper. As demonstrated in Fig.5, the continuum emission component in the measured OES for the given time range is small, and hence is not removed from the OES signal during the temperature deduction process.

4.2 Physics-based Modeling Results and Comparison with Experiments

In Fig. 4, the middle and right columns show the contour plots of the model-predicted gaseous phase temperature and density, respectively, from t = 15 to 45 ns. Figure 7 shows the model-predicted plasma top front propagation in comparison with that estimated from the ICCD images. Some model-experiment differences do exist, which is reasonable considering that the simulated process is very complicated and the model is based on simplified assumptions made to get an affordable computational cost. On the other hand, the model-experiment agreement is still within an acceptable range. In Fig.4, the model predictions at t = 15 and 20 ns show reasonably high temperatures and densities in the plasma plume's bottom region, consistent with the ICCD

images at t = 15 and 20 ns, showing the plume bottom has reasonably high brightness. On the other hand, the model predictions after t = ~30 ns show relatively low temperatures and densities in the plume's bottom region, consistent with the ICCD images after t = ~30 ns, showing the plume bottom becomes dark and appears to be separated from the powder bed surface. In Fig. 7, although the experimental curve for the plume front location initially has a larger slope than the model-predicted curve, later on the two curves become reasonably parallel, implying a similar propagation speed of the plume front. The difference in the front locations between the two curves still appear to be within an acceptable range considering the complexity of the process simulated. It should be noted that uncertainties in the experimental measurements related to the powder bed, laser pulses and/or the ICCD imaging system might also contribute to the model-experiment difference shown in Fig. 7.

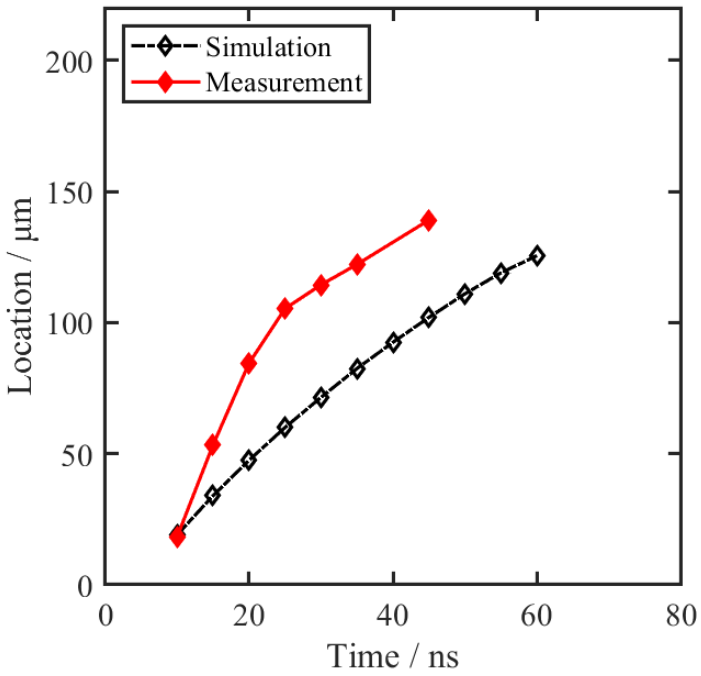

Figure 7. The plasma top front propagation predicted from the model compared with that estimated from the ICCD images.

It should be noted that for Fig.7 the earliest moment at which an ICCD image is taken is t = 10 ns. At t = 10 ns, Fig.7 shows the plasma plume already has a certain size. Thus, it is expected that plasma plume is formed at t < 10 ns. Plume images before t = 10 ns were not taken, because the plume size is expected to be very small (top front location smaller than ~20 μm) and likely the images will not provide very useful additional information for the purpose of this study.

Figure 8 shows the model-predicted plasma temperature evolution with time, in comparison with the experimentally deduced temperature (the excitation temperature of neutral cobalt atoms in the plasma). In the OES measurement, the ICCD gate is open from t = 35 to 75 ns, represented by the time error bar. The model-predicted temperature plotted is the weighted spatial average of the cobalt vapor temperature with the averaging method detailed in the "Supplemental Material" file. The simulation result in Fig. 8 shows that the temperature first increases with time, reaches the peak value and then decreases with time. The temperature predicted by the model is reasonably close to that measured in the experiment.

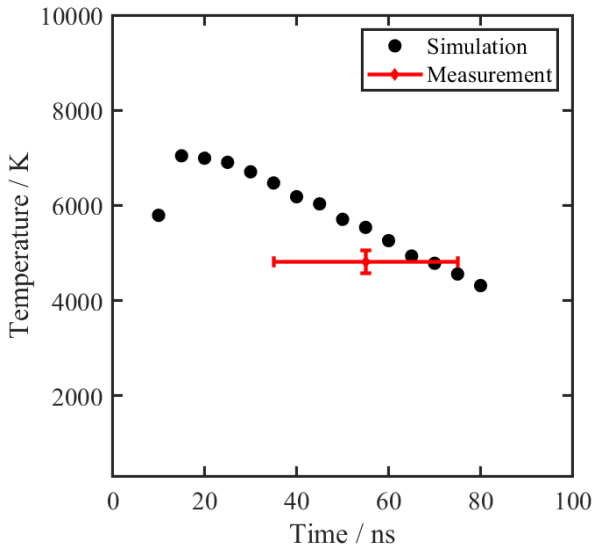

Figure 8. The plasma temperature (the weighted average values in space for cobalt vapor as introduced in the paper text) predicted by the model in comparison with that deduced from the OES measurement.

In summary, Figs. 4 and 7-8 show the model-experiment comparisons in different aspects. Although some deviations do exist, overall the model-experiment agreements still appear to be acceptable for the main purpose of this study, which is to use the model to reveal how to analyze the effect of the plasma-induced pressure on the sintering result in DP-LMS and reveal the effect of the "sintering pulses" on the plasma evolution. These will be introduced in the next two sections.

4.3 Model Analysis of Plasma Pressure Effect on the Sintering Quality in DP-LMS

Transient pressure is induced onto the powder bed surface due to the plasma generated during DP-LMS. The plasma-induced pressure on the powder bed surface plays a key role in DP-LMS and significantly affects the sintering result. Figure 9a shows the optical microscopic image of a surface region sintered by DP-LMS, in comparison with that sintered by the single-pulse laser micro sintering (SP-LMS) process in Fig.9b using only the low-intensity "sintering laser pulses" without plasma produced by the "pressing laser pulse". The region is sintered by sending one laser pulse group to each of the 3 × 3 locations as shown in Fig.9c. It can be seen from Fig.9a that the surface region sintered by the DP-LMS process utilizing the pressing pulse energy equal to ~0.12 mJ appears reasonably continuous and densified, while that by SP-LMS shows serious "balling", i.e., molten powder material shrinks into individual (near) spherical balls and then re-solidifies. As already qualitatively explained in the authors' previous papers [12, 13, 15], the plasma-induced pressure in DP-LMS, if high enough, can promote the melt flow, push the melt into a relatively continuous layer, and greatly reduce balling.

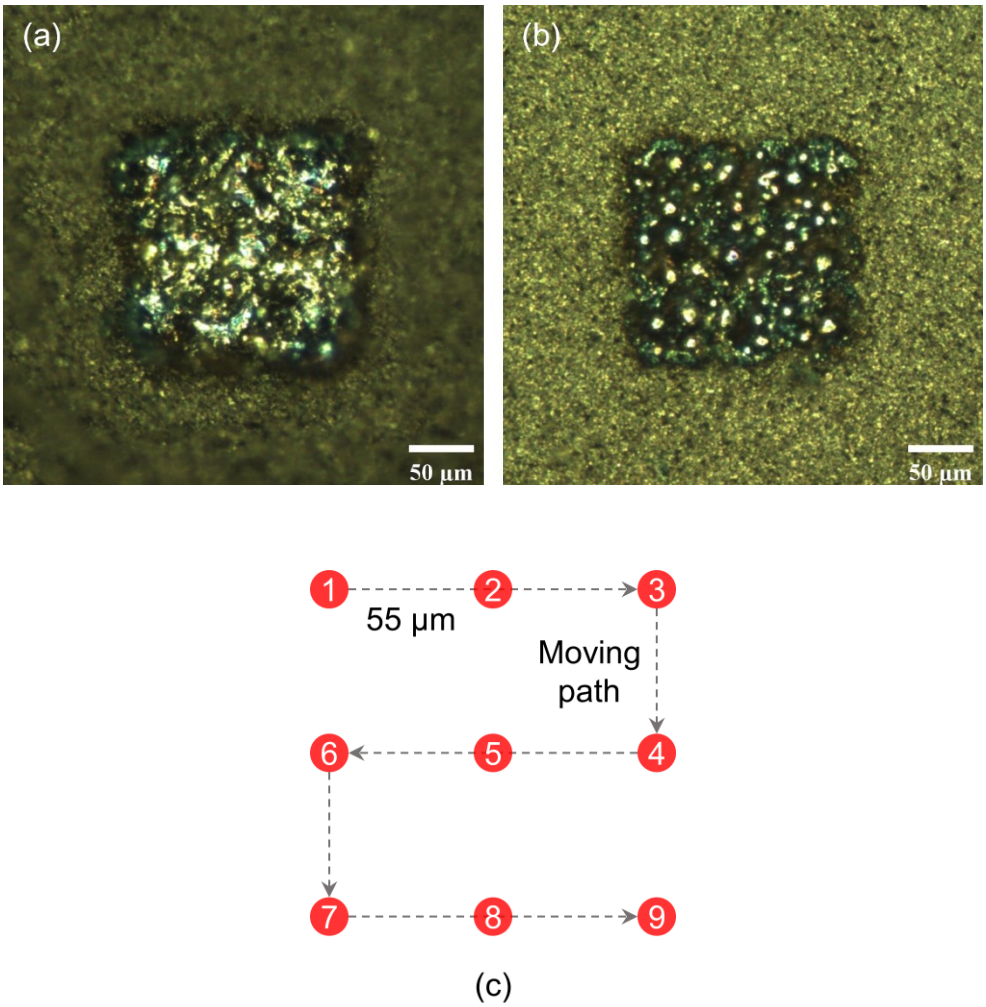

Figure 9. Optical micrographs of regions sintered via DP-LMS utilizing a pressing pulse energy of ~0.120 mJ (a) and via SP-LMS using only sintering laser pulses (b); the regions are sintered through laser irradiation of the 3×3 spot array shown in the schematic diagram in (c).

Figure 10 shows the in-situ images of the powder bed surface around the laser-irradiated region during (a) DP-LMS and (b) SP-LMS processes taken using the setup in Fig. 2. For Fig. 10a, the image capturing starts at ~6.3 µs after the pressing pulse in a laser pulse group, while for Fig. 10b, the image capturing starts at ~6.3 µs after the last sintering pulse in a laser pulse group. The cobalt material at elevated temperatures has more significant light emission and appears bright in the images. In Fig.10a, the bright region appears reasonably continuous and overall the brightness level appears reasonably uniform within the bright region. On the other hand, Figure 10b shows

multiple near-circular bright spots, separated by dark regions, implying "balling" has likely occurred. The melted cobalt particles coalesce and evolve into individual "balls", leading to poor material continuity upon solidification as demonstrated in Fig. 9b.

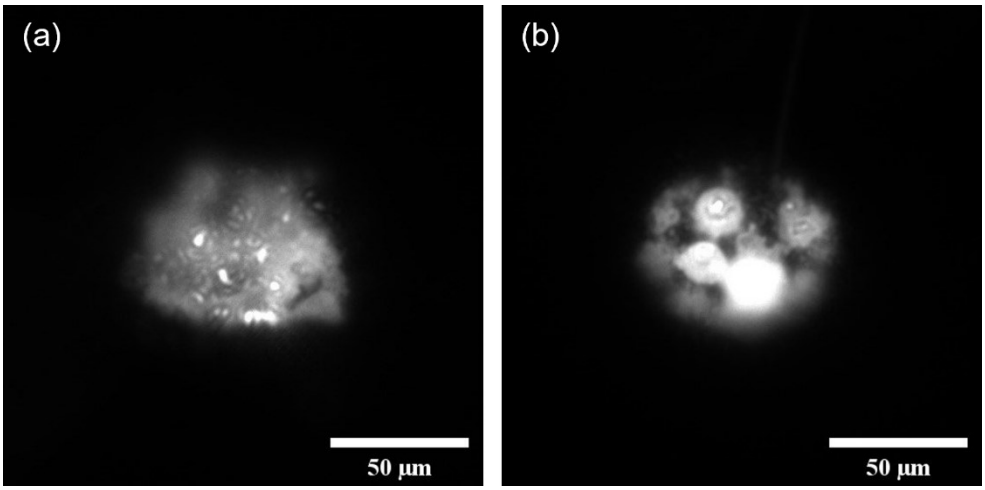

Figure 10. Images of the powder bed surface around the laser irradiated region during (a) DP-LMS and (b) SP-LMS.

In this paper, using the experimentally verified physics-based model for the plasma in DP-LMS as a tool, a further analysis will be performed about the effect of the plasma-induced pressure on balling in DP-LMS. Figure 11a shows the sintering results by DP-LMS using different pressing pulse energies from ~0.089 to ~0.120 mJ. The sintering result looks reasonably good at ~0.120 and ~0.103 mJ, although the quality of the latter is slightly worse with a little more significant balling. However, when the pressing pulse energy drops to ~0.089 mJ, obvious balling starts showing up in the sintered region. The deterioration of the sintering quality should be due to the plasma pressure reduction as the pressing pulse energy decreases. Figure 11b shows the model-predicted distribution of the total pressure exerted on the surface of the powder bed for DP-LMS utilizing different pressing laser pulse energies (for t = 6 ns, at or near which the pressure at r = 0 approximately reaches the peak value in time). The total pressure P_{tot} is the pressure of the

condensed phase right below the interface of the condensed and gaseous phases. Based on the mass and moment conservations at the interface it can be calculated as: $P_{tot} \cong P + \rho V_z^2$, where P, ρ and V_z are the gaseous phase pressure, density and z-direction velocity, respectively, at the point right above the Knudsen layer at the powder bed surface (their values at the first row of numerical grid points above the powder bed surface are used in calculating P_{tot} in this paper). It can be seen that with the pressing pulse energy of ~0.120 mJ, the pressure induced at r = 0 is around 164 MPa. It drops to around 83 MPa when the pressing pulse energy is decreased to ~0.089 mJ. As detailed in the "Supplemental Material" file, the laser-induced radiation pressure [94] is found to be insignificant and not considered.

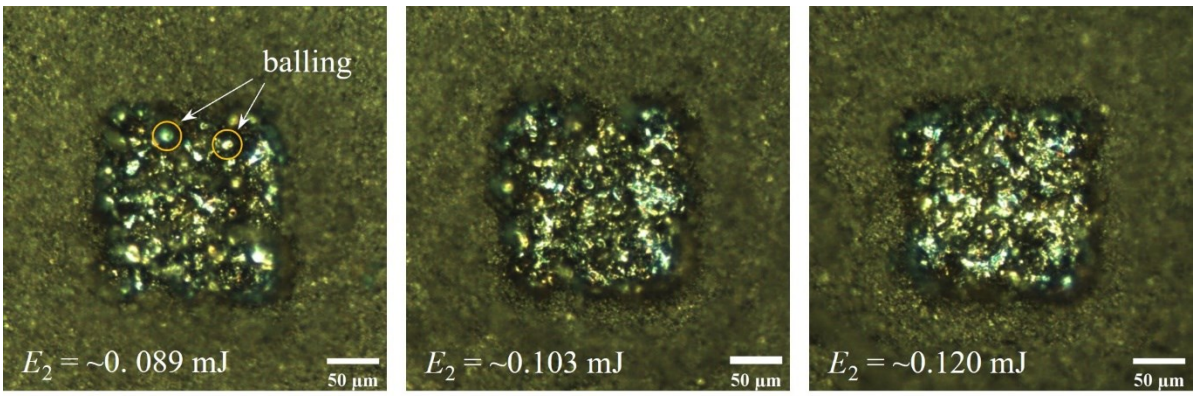

(a)

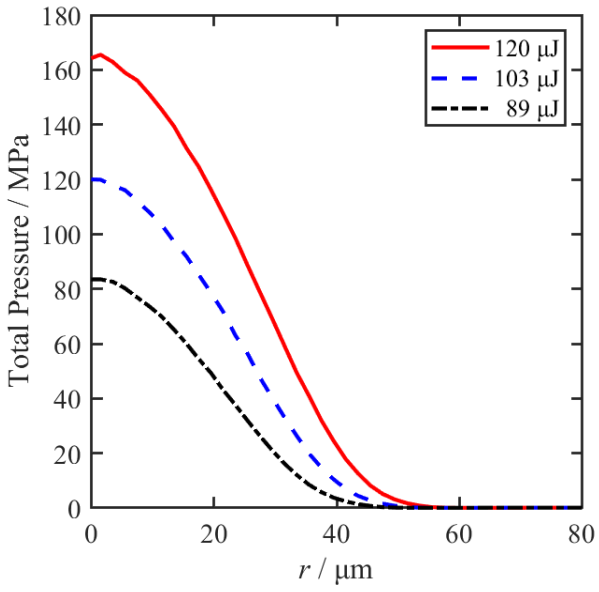

(b)

Figure 11. (a) Optical micrographs of regions sintered via DP-LMS using various pressing pulse energies (E_2) as labeled; and (b) The model-predicted distribution of the total transient pressure induced on the powder bed's surface due to laser-generated plasma during DP-LMS using various pressing pulse energies (the plots are for t = 6 ns, at or near which the pressure at r = 0 approximately reaches the peak value in time).

The pressure due to laser-induced plasma can impact the melt balls that might be formed due to melt flow driven by surface tension [95]. When the pressure is high enough, it can press a melt ball into a flat layer of molten material, reducing the balling phenomenon in the re-solidified material layer. However, the major question is: what is the minimum plasma-induced pressure

required to effectively suppress obvious balling during DP-LMS? This question will be analyzed below with the help of the DP-LMS plasma model.

As shown in Fig.12, the impact of a pressure pulse with a magnitude of *P* on a melt ball (a liquid droplet) can be analyzed with a rough analogy to an approximately similar process of a liquid droplet impacting a solid surface at a velocity *V*, a problem that has been studied in the literature [96-98]. The value of *P* and *V* can be approximately related by the relation: $P \approx \rho C_s V$ [98-100], where ρ and C_s are the density and shock speed of the liquid, respectively (the shock speed is close to the sound speed when the pressure is not very high). The analogy and the P-V relation are certainly rough, but should be sufficient for the following scale analysis.

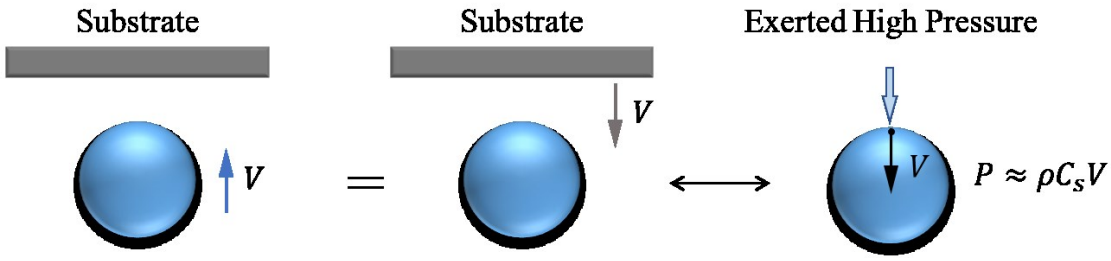

Figure 12. Schematic illustrating the rough, but reasonable analogy between the process of a pressure pulse impacting a liquid droplet and the process of the liquid droplet impacting a solid substrate surface.

After a droplet impacts a surface, its subsequent evolution process on the surface can be analyzed based on dimensionless numbers, one of which is the Weber number *We* [96, 97]:

$$We = \frac{\rho V^2 L}{\sigma} \qquad (5)$$

where *L* is the droplet radius [96] or diameter [97], σ denotes the liquid surface tension and ρ is the liquid density. The Weber number indicates the significance of the impact relative to the surface tension on the droplet evolution. When $We >> 1$, the droplet evolution process is mainly

impact driven (i.e., the process is mainly driven by the impact pressure); when $We << 1$, the droplet evolution is mainly capillarity force driven [96].

For a given pressing laser pulse energy in DP-LMS, the plasma peak pressure P can be calculated using the physics-based model. Then the velocity V of the approximately analogized process of a droplet impacting a solid surface can be estimated via the aforementioned relation $P \approx \rho C_s V$ [98-100], where the molten cobalt speed of sound is taken from [101]. Then the Weber number can be calculated using Eq.(5), where the surface tension of molten cobalt at the melting point from [102] is employed, and the droplet diameter is used for L and assumed to be 10 μm. The assumed value of the droplet diameter is estimated based on the order of magnitude of the typical diameters of balls in the optical microscopic image of the region sintered by SP-LMS in Fig.9b. In this way, the Weber number of the analogized droplet impact process can be calculated for DP-LMS with various pressing pulse energies, and is plotted in Fig.13.

Figure 13 shows that under the studied conditions the Weber number is on the order of magnitude close to ~1, implying that both the pressure impact and the molten material surface tension play noticeable roles in the melt droplet evolution. According to the physical implication of Weber number, when it is much less than 1, the surface tension has a more significant effect than the pressure impact on the melt droplet evolution [96] and obvious balling in the sintering result is expected. This is consistent with Fig. 13, showing that with a pressing pulse of ~0.089 mJ, We is less than 0.3, and the micrograph of the sintered region shows obvious balling. As Weber number increases, according to its physical implication, the effect of the pressure impact increases. Figure 13 shows that the DP-LMS result does not show significant balling when We exceeds ~1. Hence, under the studied particular conditions, Figure 13 suggest that in DP-LMS the minimum plasma-induced pressure required to effectively suppress balling for a good sintering

quality is approximately the pressure making the Weber number exceed ~1 for the approximately analogized process of a droplet impacting a solid surface.

The DP-LMS results in Figs.9, 11 and 13 are for a simple situation of sintering 3 × 3 points with a stationary laser spot for each point. Such a simple situation is chosen to facilitate the discussion using the model. Refs. [13] and [15] report the authors' previous experimental studies on single-track and multiple-track DP-LMS, respectively, and have scanning electron microscopic (SEM) images of material sintered by DP-LMS in comparison with that by SP-LMS.

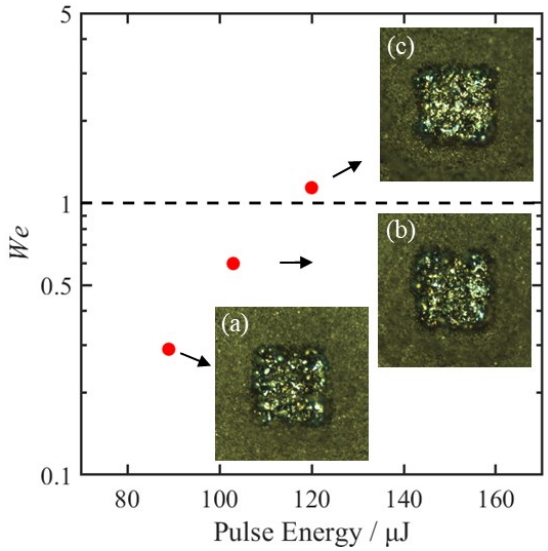

Figure 13. The Weber number of the approximately analogized droplet impact process for DP-LMS using various pressing laser pulse energies (the Weber number is calculated based on the model-predicted total pressure at r = 0 for t = 6 ns, at or near which the total pressure at r = 0 approximately reaches the peak value in time).

The "Pressing Pulse Stage Module" is based on the surface evaporation mechanism, whose validity requires the peak temperature of the powder bed surface to be lower than the thermodynamic critical temperature of cobalt (which is ~10,384 K [103]). The simulations under the studied conditions show that this condition has been satisfied.

4.4 The Effect of Sintering Pulses on Plasma Evolution

Although the plasma in DP-LMS is generated by the pressing pulse, the preceding sintering pulses in the same pulse group may also affect the plasma evolution by two mechanisms: (1) elevating the powder bed temperature and (2) changing the ambient air condition when the pressing pulse arrives.

Mechanism (1) is very easy to understand, while Mechanism (2) is demonstrated in Fig. 14, showing the model-predicted temperature and density contour plots of air right before the "pressing laser pulse" arrives. The "sintering laser pulses" heat the powder in the surface layer of the powder bed, which then heats the air in the pores of the powder bed and the air above the powder bed surface. The hot air expands, causing a high-temperature and low-density air zone above the laser spot center on the powder bed as shown in Fig.14. The reduced air density will affect the subsequent evolution of the plasma generated by the pressing laser pulse.

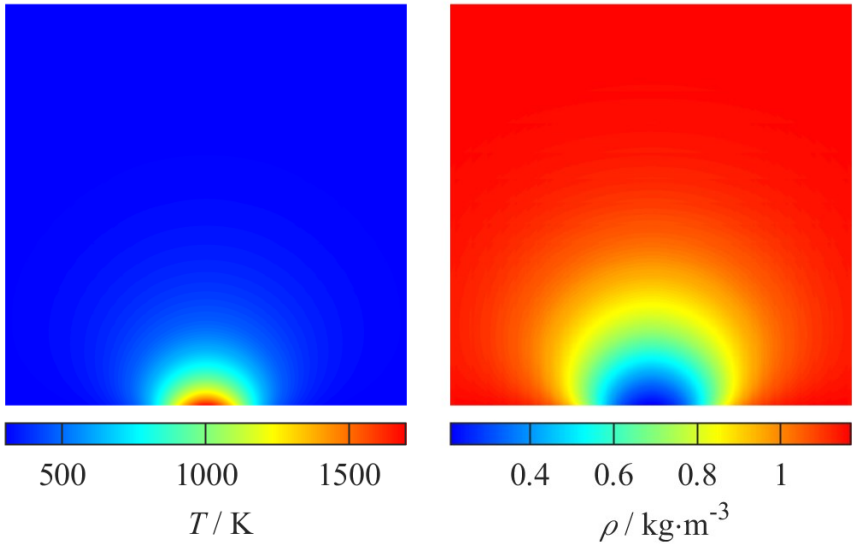

Figure 14. The model-predicted air temperature and density distributions above the laser-irradiated location of the powder bed surface right before the pressing laser pulse arrives (each plot corresponds to an actual domain of 300 μm × 300 μm, excluding the powder bed- ambient air interface).

In DP-LMS, the major purpose of the "pressing laser pulse" is typically to produce plasma to generate high pressure on the surface of the powder bed in order to promote melt flow, and thus to alleviate balling and improve densification for the sintered material. Hence, the laser-induced pressure at the powder surface critically influences the laser sintering result. Figure 15a and b show the pressure history at two points of the powder bed surface (the $r = 0$ and $r = 20$ μm points) for the "double pulse" (i.e., DP-LMS) and "pressing-pulse-only" situations, respectively. In the DP-LMS situation, the powder bed is irradiated by 10 sintering pulses followed by 1 pressing pulse, while in the "pressing-pulse-only" situation, the powder bed is only irradiated by 1 pressing pulse. In each situation, the time $t = 0$ for Fig. 15 is defined as the moment of the pressing pulse's arrival. Figure 15 shows that the peak pressures in time at $r = 0$ and 20 μm for the DP-LMS situation are obviously higher than those for the "pressing-pulse-only" situation.

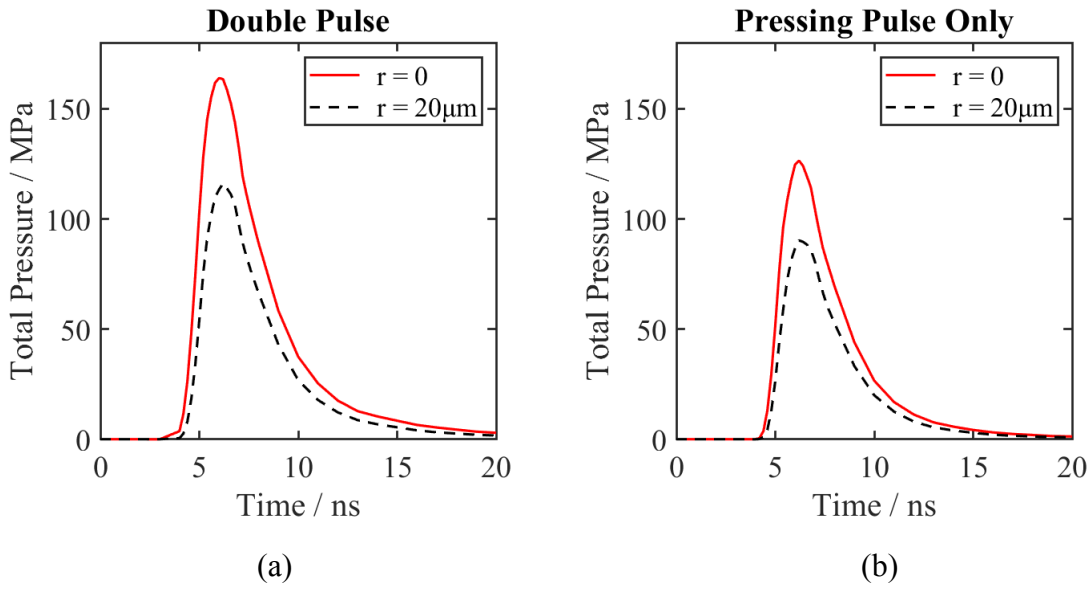

Figure 15. The model-predicted total pressure exerted on the surface of the condensed phase of the powder bed for the situations of (a) DP-LMS (i.e., 10 sintering pulses followed by 1 pressing pulse) and (b) only using one pressing pulse.

Figure 16 shows the accumulated evaporation mass from the powder bed surface for the DP-LMS and the pressing-pulse-only situations. The arrival of the pressing pulse is still defined as $t = 0$ for the figure. In both situations, the accumulated mass first quickly increases with time and then saturates, with the saturation occurring earlier for the pressing-pulse-only situation. The accumulated evaporation mass for the DP-LMS situation is obviously larger than that for the pressing-pulse-only situation. In the former situation, the evaporated mass exceeds 1.1×10^{-12} kg by $t = 20$ ns, while in the latter situation, the evaporated mass is only slightly larger than 0.8×10^{-12} kg by $t = 15$ ns.

Compared with the pressing-pulse-only situation, the higher powder bed surface pressure and larger amount of evaporated mass for DP-LMS shown in Figs.15 and 16 are mainly due to Mechanism (1) mentioned earlier. Mechanism (1) is found to play the major role here, because the simulation considering only Mechanism (1) without Mechanism (2) gives results on the pressure and accumulated evaporation mass very similar to those for DP-LMS in Figs.15 and 16.

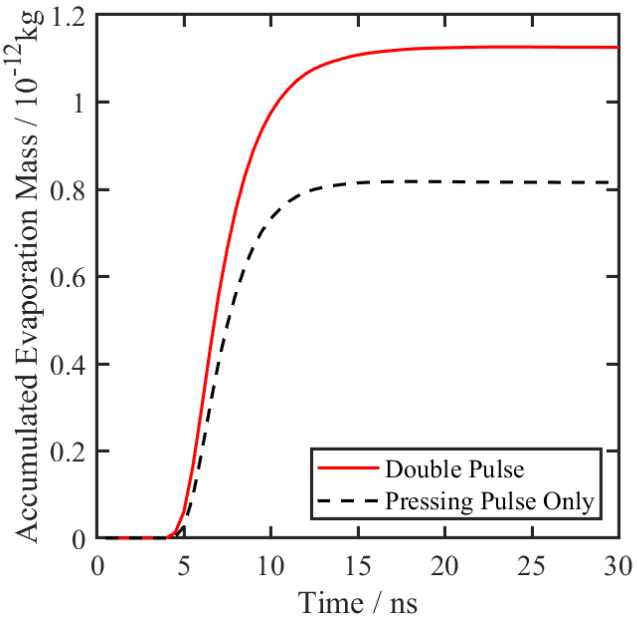

Figure 16. The accumulated evaporation mass from the powder bed surface predicted by the model for the situations of DP-LMS and only using one pressing pulse.

Figure 17 shows the model-predicted pressure and velocity distributions in z direction at r = 0 for t = 6 and 10 ns in the gaseous phase for the situations of DP-LMS and only using the pressing pulse. The first row of the figure shows the pressure distributions. It can be seen that at t = 6 ns and 10 ns, the pressures near z = 0 (the powder bed surface) are obviously higher for the DP-LMS situation than those for the pressing-pulse-only situation. The front of the elevated pressure also propagates faster in the former situation than the latter situation. The second row of Fig. 17 shows the z-direction velocity (U_z) distribution. The values of U_z near z = 0 at t = 6 ns and 10 ns for the DP-LMS situation are close to those for the pressing-pulse-only situation at t = 6 ns and 10 ns, respectively. However, the spatially peak values of U_z along the line of r = 0 at t = 6 ns and 10 ns for the DP-LMS situation are obviously larger than those for the pressing-pulse-only situation at t = 6 ns and 10 ns, respectively. The front of the elevated velocity propagates faster in the former situation than the latter situation.

Based on the simulation for DP-LMS considering both Mechanisms (1) and (2) and the simulation for DP-LMS only considering Mechanism (1) without Mechanism (2), it has been found that the higher pressure near z = 0 for DP-LMS in Fig.17 is mainly due to Mechanism (1). On the other hand, both Mechanisms (1) and (2) play a role in the faster propagation of the fronts of the elevated pressure and velocity and in the higher spatial peak values of U_z for DP-LMS.

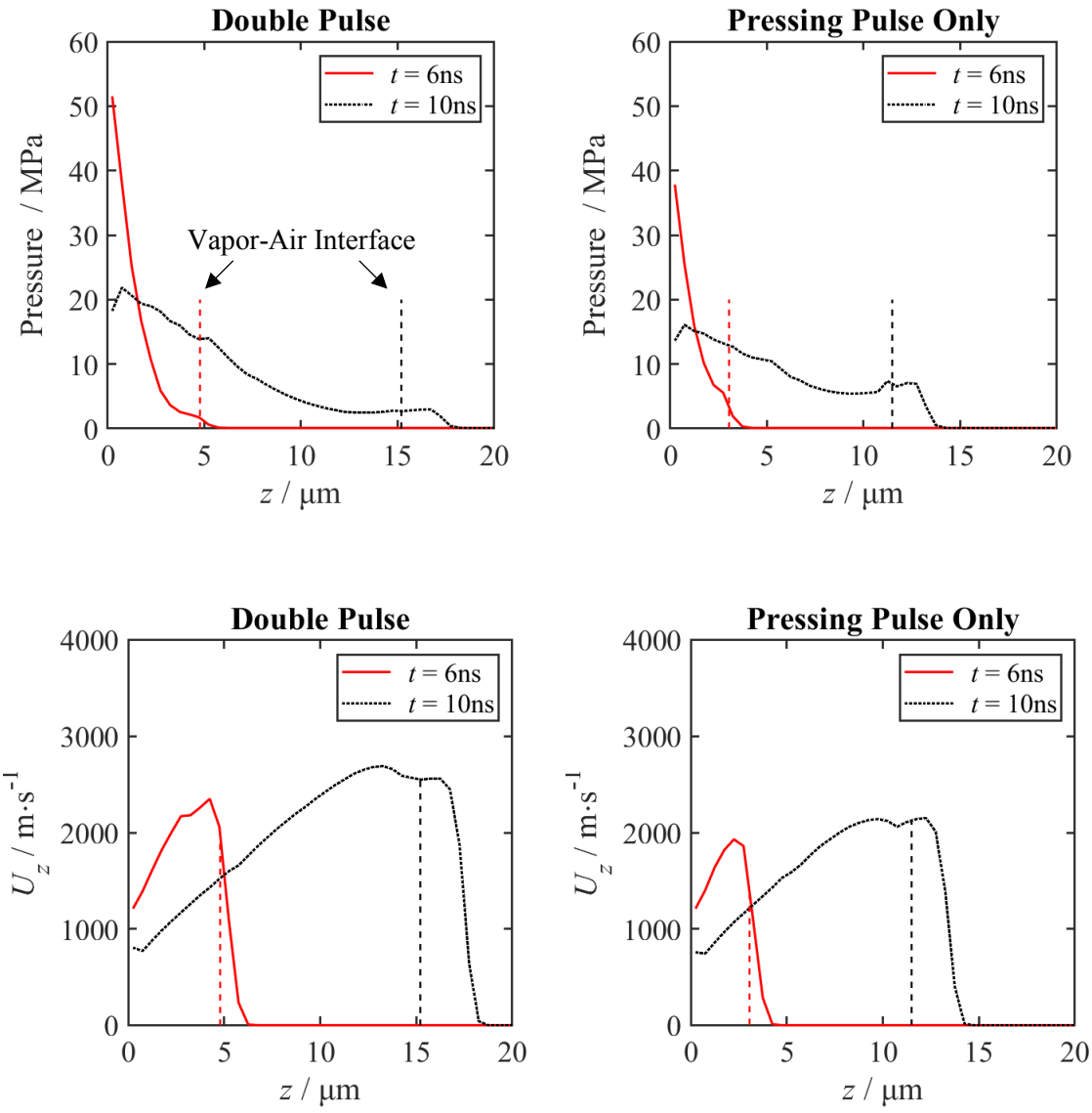

Figure 17. The model-predicted pressure and z-direction velocity (U_z) distributions along z at r = 0 in the gaseous phase for the DP-LMS and pressing-pulse-only situations.

In DP-LMS, whether or not the plasma-induced pressure on the powder bed surface can effectively suppress balling depends on the relative significance of the pressure compared with the surface tension of the molten metal, which can be analyzed based on the Weber number as shown earlier. Figure 18 compares the Webber numbers calculated based on the model-predicted pressures for the DP-LMS and pressing-pulse-only situations. Figure 18 shows that with different pressing pulse energies, the Weber number calculated for the DP-LMS situation is much larger than that for the pressing-pulse-only situation. The comparison suggests that the "sintering laser pulses" in DP-LMS can have an obvious effect on the plasma, and such an effect needs to be considered in modeling the plasma to simulate its evolution more accurately, particularly for purpose of analyzing the effect of the plasma on the sintering result via the Weber number.

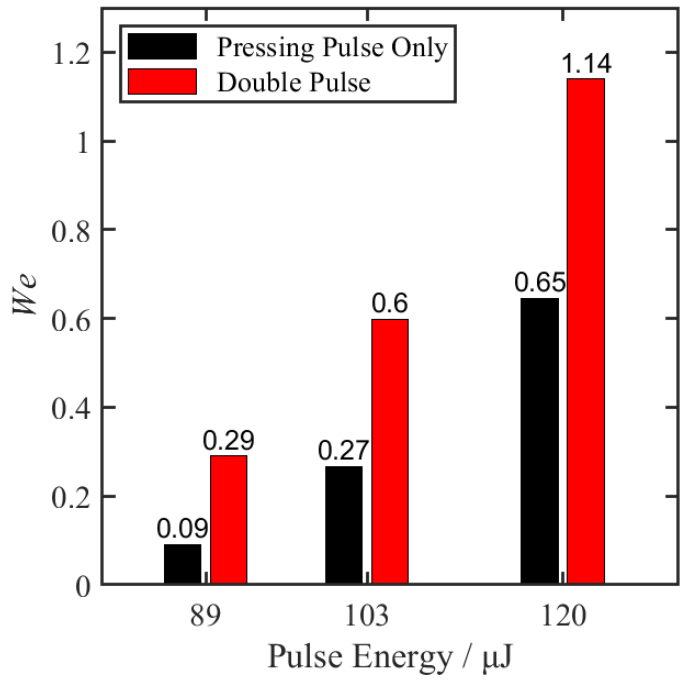

Figure 18. The Weber numbers calculated based on the model-predicted total pressures exerted on the powder bed surface at r = 0 and t = 6 ns (at or near which the pressure at r = 0 approximately reaches the peak value in time) for the DP-LMS and pressing-pulse-only situations for different pressing pulse energies.

Some additional information is given in the "Supplemental Material" file, including (but not necessarily limited to) additional details for the model, the discussions on simplified assumptions, the justification of using one-temperature gas dynamic equations for the "Pressing Pulse Stage Module" and the justification of the model-experiment comparison in Fig.8 based on the neutral particle collision time [69, 77, 104, 105,], the electron-heavy particle energy relaxation time [69, 77] and the McWhirter's criterion [34, 37, 38, 106]. Finally, it should be noted that there is certainly room for the improvement of the model in this paper, which is based on some simplified assumptions intended to get an acceptable computational cost.

5. Conclusions

This paper has reported an experiment-model integrative study, combining time-resolved imaging and OES measurements with physics-based modeling, for plasma induced during DP-LMS, a novel laser micro sintering process proposed previously [14]. The plasma top front propagation and temperature obtained from the measurements are compared with those predicted by the model for its verification. The tested model is then used to further analyze the effect of the plasma-induced pressure on the sintering quality of DP-LMS and the effect of the sintering pulses on the plasma. For the related conditions that have been investigated in this paper, the major discoveries are summarized below:

(1) Although some model-experiment deviations do exist, the overall model-experiment agreements for the plasma top front propagation and temperature are still within an acceptable range for the major purpose of this study.

(2) Both the in-situ image of the powder bed surface in DP-LMS and the post-process optical micrograph of the sintered region show that the plasma-induced pressure, if high enough, can suppress balling and increase densification in the sintered material.

(3) The Weber number for the analogized process of a droplet impacting a solid surface can be utilized to analyze the effect of the plasma-induced pressure on the sintering quality in DP-LMS. Under the studied conditions, the minimum pressure required to effectively suppress balling for a good sintering quality is approximately the pressure making the Weber number exceed ~1.

(4) In DP-LMS, the "sintering pulses" can affect the evolution of the plasma induced by the following "pressing pulse" by (i) elevating the powder bed temperature and (ii) creating a hot, low-density air region above the laser spot center on the surface of the powder bed when the pressing laser pulse arrives. The effect of the "sintering pulses" can obviously increase the plasma-induced pressure on the powder bed surface that plays a key role in the sintering quality.

Declaration of Competing Interest

As already introduced earlier, Prof. Benxin Wu (the corresponding author for this paper) is the inventor of the approved patent about double-pulse laser micro sintering as introduced in Ref. [14].

Acknowledgment

This material is based upon work supported by the National Science Foundation under Grant No. CMMI 1728481. The NSF award's grantee is Purdue University (West Lafayette, Indiana, USA).

List of References

1. J.J. Beaman, D.L. Bourell, C.C. Seepersad, D. Kovar, Additive manufacturing review: Early past to current practice, Journal of Manufacturing Science and Engineering, 142 (2020) 110812.
2. W.E. King, A.T. Anderson, R.M. Ferencz, N.E. Hodge, C. Kamath, S.A. Khairallah A.M. Rubenchik, Laser powder bed fusion additive manufacturing of metals; physics, computational, and materials challenges, Applied Physics Reviews, 2 (2015) 041304.
3. G. Gong, J. Ye, Y. Chi, Z. Zhao, Z. Wang, G. Xia, X. Du, H. Tian, H. Yu, C. Chen, Research status of laser additive manufacturing for metal: a review, Journal of Materials Research and Technology, 15 (2021) 855-84.
4. P. Fischer, M. Locher, V. Romano, H.P. Weber, S. Kolossov, R. Glardon, Temperature measurements during selective laser sintering of titanium powder, International Journal of Machine Tools and Manufacture, 44 (2004) 1293-1296.
5. L. Caprio, A.G. Demir, B. Previtali, Influence of pulsed and continuous wave emission on melting efficiency in selective laser melting, Journal of Materials Processing Technology, 266 (2019) 429-441.
6. H. Song, Z. Kang, B. Wu, Nanosecond pulsed laser sintering of carbon nanotube–Silver nanocomposite thin films on a flexible substrate: In-situ temperature measurements and post-process characterizations, Journal of Manufacturing Processes, 79 (2022) 476-85.
7. H. Song, M. Wu, W. Liu, B. Wu, Thermal modeling and validation via time-resolved temperature measurements for nanosecond laser irradiation of a powder bed of micro metal particles, Optics & Laser Technology, 152 (2022) 107981.
8. A. Streek, P. Regenfuss, R. Ebert, H. Exner, Laser micro sintering–a quality leap through improvement of powder packing, 2008 International Solid Freeform Fabrication Symposium.
9. G. Jacob, C.U. Brown, A. Donmez, The influence of spreading metal powders with different particle size distributions on the powder bed density in laser-based powder bed fusion processes, Gaithersburg, MD: US Department of Commerce, National Institute of Standards and Technology, 2018.
10. S.E., Brika, M. Letenneur, C.A. Dion, V. Brailovski, Influence of particle morphology and size distribution on the powder flowability and laser powder bed fusion manufacturability of Ti-6Al-4V alloy, Additive Manufacturing, 31 (2020) 100929.
11. P. Regenfuss, A. Streek, L. Hartwig, S. Klötzer, Th. Brabant, M. Horn, R. Ebert, H. Exner, Principles of laser micro sintering, Rapid Prototyping Journal, 13 (2007) 204-212.
12. H. Song, Z. Kang, Z. Liu, B. Wu, Experimental study of double-pulse laser micro sintering: A novel laser micro sintering process, Manufacturing letters, 19 (2019) 10-14.
13. W. Liu, H. Song, B. Wu, H. You, Double-pulse laser micro sintering: Experimental study and mechanism analysis aided by in-situ time-resolved temperature measurements, Journal of Manufacturing Processes, 69 (2021) 191-203.
14. B. Wu, inventor; Purdue Research Foundation, assignee. Processes and systems for double-pulse laser micro sintering. United States patent. Patent No.: US11,440,099 B2. Date of Patent: 09/13/2022 (related provisional patent application number: 62693684, filed on 07/03/2018).
15. W. Liu, B. Wu, R. Cui, H. Wang, S. Liu, M. Asheroo, H. Song, Double-pulse laser micro sintering of iron powder in multiple overlapping tracks: experimental study and material characterizations, Journal of Manufacturing Processes, 99 (2023) 405-415.

16. H. Song, W. Liu, B. Wu, Physics-based computational modeling and time-resolved imaging of plasma plume generated by nanosecond laser interaction with a bed of micro metallic powder, Additive Manufacturing, 58 (2022) 102984.
17. D. Cheng, H. Zhu, L. Ke, Investigation of plasma spectra during selective laser micro sintering Cu-based metal powder, Rapid Prototyping Journal, 19/5 (2013) 373-382.
18. S.G. Demos, R.A. Negres, R.N. Raman, N. Shen, A.M. Rubenchik, M.J. Matthews, Mechanisms governing the interaction of metallic particles with nanosecond laser pulses, Optics Express, 24 (2016) 7792-7815.
19. X.L. Li, Y.J. Li, S.T. Li, M.J. Zhou, L.W. Chen, J. Meng, D.B. Qian, J. Yang, S.F. Zhang, Y. Wu, X.W Ma, Steplike behavior in grain-size-dependent optical emission of plasma induced by laser-ablating granular material, Physical Review Applied, 16 (2021) 024017.
20. P. Bidare, L. Bitharas, R.M. Ward, M.M. Attallah, A.J. Moore, Fluid and particle dynamics in laser powder bed fusion, Acta Materialia, 142 (2018) 107-120.
21. C.S. Lough, L.I. Escano, M. Qu, C.C. Smith, R.G. Landers, D.A. Bristow, L. Chen, E.C. Kinzel, In-situ optical emission spectroscopy of selective laser melting. Journal of Manufacturing Processes, 53 (2020) 336-41.
22. S. S. Harilal, M. C. Phillips, D. H. Froula, K. K. Anoop, R. C. Issac, and F. N. Beg, Optical diagnostics of laser-produced plasmas, Reviews of Modern Physics, 94 (2022) 035002.
23. K. Pangovski, S. Martin, and O.N. William, A holographic method for optimisation of laser-based production processes, Advanced Optical Technologies, 5 (2016) 177-186.
24. T.E. Itina, J. Hermann, P. Delaporte, and M. Sentis, Laser-generated plasma plume expansion: Combined continuous-microscopic modeling, Physical Review E, 66 (2002) 066406.
25. A. Bogaerts and Z. Chen, Effect of laser parameters on laser ablation and laser-induced plasma formation: A numerical modeling investigation, Spectrochimica Acta Part B: Atomic Spectroscopy, 60 (2005) 1280-1307.
26. Capitelli, M., A. Casavola, G. Colonna, and Alessandro De Giacomo. "Laser-induced plasma expansion: theoretical and experimental aspects." Spectrochimica Acta Part B: Atomic Spectroscopy, 59 (2004) 271-289.
27. Callies, Gert, Peter Berger, and Helmut Hugel. "Time-resolved observation of gas-dynamic discontinuities arising during excimer laser ablation and their interpretation." Journal of Physics D: Applied Physics, 28 (1995) 794-806.
28. A. Gupta, B. Braren, K. G. Casey, B. W. Hussey, and Roger Kelly. Direct imaging of the fragments produced during excimer laser ablation of $YBa_2Cu_3O_{7-\delta}$, Applied physics letters, 59 (1991) 1302-1304.
29. S. Donadello, A. G. Demir, and Barbara Previtali. Probing multipulse laser ablation by means of self-mixing interferometry, Applied Optics 57 (2018) 7232-7241.
30. S. Donadello, F. Valentina, A. G. Demir, B. Previtali. Time-resolved quantification of plasma accumulation induced by multi-pulse laser ablation using self-mixing interferometry, Journal of Physics D: Applied Physics, 53 (2020) 495201.
31. V. Narayanan, V. Singh, Pramod K. Pandey, Neeraj Shukla, and R. K. Thareja, Increasing lifetime of the plasma channel formed in air using picosecond and nanosecond laser pulses, Journal of Applied Physics, 101 (2007) 073301.
32. O.A. Ranjbar, Z. Lin, and A. N. Volkov, Plume accumulation effect and interaction of plumes induced by irradiation of a copper target with a burst of nanosecond laser pulses near the ionization threshold, Journal of Applied Physics, 127 (2020) 223105.

33. A.H. Fleitman, R.B. Herchenroeder, J.G.Y. Chow, Cobalt-base alloys for use in nuclear reactors, Nuclear Engineering and Design, 15 (1971) 345-62.
34. M. Sabsabi, P. Cielo, Quantitative analysis of aluminum alloys by laser-induced breakdown spectroscopy and plasma characterization, Applied Spectroscopy, 49 (1995) 499-507.
35. A. Ciucci, M. Corsi, V. Palleschi, S. Rastelli, A. Salvetti, E. Tognoni, New procedure for quantitative elemental analysis by laser-induced plasma spectroscopy, Applied spectroscopy, 53 (1999) 960-4.
36. J.B. Simeonsson, A.W. Miziolek, Time-resolved emission studies of ArF-laser-produced microplasmas, Applied Optics, 32 (1993) 939-47.
37. J. Hou, L. Zhang, W. Yin, Y. Zhao, W. Ma, L. Dong, G. Yang, L. Xiao, S. Jia, Investigation on spatial distribution of optically thin condition in laser-induced aluminum plasma and its relationship with temporal evolution of plasma characteristics, Journal of Analytical Atomic Spectrometry, 32 (2017) 1519-26.
38. M.A. Khan, S. Bashir, N.A. Chishti, E. Bonyah, A. Dawood, Z. Ahmad, Effect of ambient environment and magnetic field on laser-induced cobalt plasma, AIP Advances, 13 (2023) 015017.
39. C. Aragón, J.A. Aguilera, Characterization of laser induced plasmas by optical emission spectroscopy: A review of experiments and methods, Spectrochimica Acta Part B, 63 (2008) 893-916.
40. V. Anand, A. Nair, A. Karur Karunapathy Nagendirakumar, M.R. Gowravaram, Estimating the number density and energy distribution of electrons in a cold atmospheric plasma using optical emission spectroscopy, Journal of Vacuum Science & Technology A, 36 (2018) 04F407.
41. A.P. Thorne, Spectrophysics, Chapman and Hall Ltd, London, 2nd edition, 1988.
42. D. Lumma. Investigation of a diagnostic technique for measuring electron densities via Stark broadening on the Alcator C-Mod tokamak, Master of Science Thesis, Massachusetts Institute of Technology, 1996.
43. Matt Newville, Renee Otten, Andrew Nelson, Antonino Ingargiola, Till Stensitzki, Dan Allan, Austin Fox, Faustin Carter, Michał, Dima Pustakhod, Yoav Ram, Glenn, Christoph Deil, Stuermer, Alexandre Beelen, Oliver Frost, Nicholas Zobrist, Mark, Gustavo Pasquevich, Allan L. R. Hansen, Tim Spillane, Shane Caldwell, Anthony Polloreno, Andrew Hannum, Jonathan Fraine, deep-42-thought, Benjamin F. Maier, Ben Gamari, Arun Persaud, Anthony Almarza, lmfit/lmfit-py 1.0.1, (2020). https://doi.org/10.5281/zenodo.3814709.
44. S. Tao, Y. Zhou, B. Wu, Y. Gao, Infrared long nanosecond laser pulse ablation of silicon: integrated two-dimensional modeling and time-resolved experimental study, Applied Surface Science, 258 (2012) 7766–7773.
45. B. Xiao, Y. Zhang, Marangoni and buoyancy effects on direct metal laser sintering with a moving laser beam, Numerical Heat Transfer, Part A: Applications, 51 (2007) 715-33.
46. V. Ankudinov, G.A. Gordeev, M.D. Krivilyov, Numerical simulation of heat transfer and melting of Fe-based powders in SLM processing, In IOP Conference Series: Materials Science and Engineering, 192 (2017) 012026.
47. The Iron Triad: Iron, Cobalt, and Nickel. (Last updated: August 25, 2020). Accessed on April 21, 2023, from https://chem.libretexts.org/@go/page/24345
48. Thermal Properties of Metals, Conductivity, Thermal Expansion, Specific Heat. https://www.engineersedge.com/properties_of_metals.htm (accessed on April 21, 2023).

49. D.S. Smith, A. Alzina, J. Bourret, B. Nait-Ali, F. Pennec, N. Tessier-Doyen, K. Otsu, H. Matsubara, P. Elser, U.T. Gonzenbach, Thermal conductivity of porous materials, Journal of Materials Research, 28 (2013) 2260-2272.
50. A.V. Gusarov, J.P. Kruth, Modelling of radiation transfer in metallic powders at laser treatment, International Journal of Heat and Mass Transfer, 48 (2005) 3423-3434.
51. A.V. Gusarov, I. Smurov, Thermal model of nanosecond pulsed laser ablation: Analysis of energy and mass transfer, Journal of Applied Physics, 97 (2005) 014307.
52. C.J. Knight, Transient vaporization from a surface into vacuum, AIAA Journal, 20 (1982) 950-4.
53. A. Miotello, R. Kelly, "Critical assessment of thermal models for laser sputtering at high fluences", Applied Physics Letters, 67 (1995) 3535-7.
54. H. Sundqvist, G. Veronis, A simple finite-difference grid with non-constant intervals, Tellus, 22 (1970) 26-31.
55. OpenFOAM - The Open Source Computational Fluid Dynamics (CFD) Toolbox, https://openfoam.org/version/7/, accessed on April 27, 2023.
56. The OpenFOAM Foundation, OpenFOAM User Guide 7, https://openfoam.org, July 2019 (also see: https://doc.cfd.direct/openfoam/user-guide-v7/).
57. H.G. Weller, G. Tabor, H. Jasak, C. Fureby, A tensorial approach to computational continuum mechanics using object-oriented techniques, Computers in Physics, 12 (1998) 620–631.
58. H. Jasak, Error analysis and estimation for the finite volume method with applications to fluid flows, PhD Thesis, University of London and Imperial College, 1996.
59. C. Greenshields, H. Weller, Notes on Computational Fluid Dynamics: General Principles, 2022, CFD Direct Ltd, Reading, UK.
60. M.J.S, De Lemos, Turbulence in porous media: modeling and applications, Elsevier, 2012.
61. N. Dukhan, Ö. Bağcı and M. Özdemir, Experimental flow in various porous media and reconciliation of Forchheimer and Ergun relations, Experimental Thermal and Fluid Science, 57 (2014) 425–433.
62. Kaviany, M. Principles of heat transfer in porous media, Springer, 2nd edition.
63. J. A. Ochoa-Tapia and S. Whitaker, Momentum transfer at the boundary between a porous medium and a homogeneous fluid—I. theoretical development, International Journal of Heat and Mass Transfer, 38 (1995) 2635–2646.
64. S. Whitaker, Simultaneous heat, mass, and momentum transfer in porous media: a theory of drying. In Advances in heat transfer, 13 (1977) 119–203, Elsevier.
65. P.J. Żuk, B. Tużnik, T. Rymarz, K. Kwiatkowski, M. Dudyński, F.C. Galeazzo, and G.C. Krieger Filho, OpenFOAM solver for thermal and chemical conversion in porous media. Computer Physics Communications, 278 (2022) 108407.
66. COMSOL, Porous Media Flow Module User's Guide, Version: 5.6.
67. K. Kadoya, N. Matsunaga, A. Nagashima, Viscosity and thermal conductivity of dry air in the gaseous phase, Journal of Physical and Chemical Reference Data, 14 (1985) 947-970.
68. https://www.engineeringtoolbox.com/air-specific-heat-capacity-d_705.html (accessed on 12/17/2023)
69. Y.B. Zel'dovich, Y.P. Raizer, Physics of Shock Waves and High-temperature Hydrodynamic Phenomena, Academic Press, New York and London, 1966-1967.
70. Poinsot, T. and Veynante, D. (2005). Theoretical and numerical combustion. RT Edwards, Inc.

71. F.L. Pedrotti, L.S. Pedrotti, L.M. Pedrotti, Introduction to Optics, Pearson Prentice Hall, 2007.
72. A.V. Gusarov, A.G. Gnedovets, I. Smurov, Gas dynamics of laser ablation: Influence of ambient atmosphere, J. Appl. Phys., 88 (2000) 4352-4364.
73. S. Gurlui, M. Agop, P. Nica, M. Ziskind, C. Focsa, Experimental and theoretical investigations of a laser-produced aluminum plasma, Phys. Rev. E., 78 (2008) 026405.
74. J.C. Tannehill, D.A. Anderson, R.H. Pletcher, Computational Fluid Mechanics and Heat Transfer, second ed., Taylor and Francis, Washington, DC, 1997.
75. M.R. Zaghloul, M.A. Bourham, J.M. Doster, A simple formulation and solution strategy of the Saha equation for ideal and nonideal plasmas, Journal of Physics D: Applied Physics, 33 (2000) 977-984.
76. L. Spitzer, Physics of Fully Ionized Gases, Interscience Publishers, Inc., New York, 1956.
77. M. Mitchner, C.H. Kruger, Partially Ionized Gases, Wiley, New York, 1973.
78. E.E. Shpilrain, Air (properties of), https://www.thermopedia.com/content/553/ (accessed on April 21, 2023)
79. Oxygen – Electron Affinity – Electronegativity – Ionization Energy of Oxygen, https://www.nuclear-power.com/oxygen-affinity-electronegativity-ionization/ (accessed on April 21, 2023)
80. Nitrogen – Electron Affinity – Electronegativity – Ionization Energy of Nitrogen, https://www.nuclear-power.com/nitrogen-affinity-electronegativity-ionization/ (accessed on April 21, 2023)
81. S.H. Jeong, R. Greif, R.E. Russo, Laser heating of metal targets including the influence of the background pressure, Proc. of the ASME Heat Transf. Division, 351 (1997) 63-73.
82. C.J. Knight, Theoretical modeling of rapid surface vaporization with back pressure, AIAA J., 17 (1979) 519-523.
83. S.I. Anisimov, Vaporization of metal absorbing laser radiation, Sov. Phys. JETP, 27 (1968) 182-183.
84. A. Peterlongo, A. Miotello, R. Kelly, Laser-pulse sputtering of aluminum:Vaporization, boiling, superheating, and gas-dynamic effects, Phys. Rev. E., 50 (1994) 4716-4727.
85. X.D. Liu, S. Osher, Convex ENO high order multi-dimensional schemes without field by field decomposition or staggered grids, J. Comput. Phys., 142 (1998) 304 – 330.
86. A.F. Guillermet, Critical evaluation of the thermodynamic properties of cobalt, International Journal of Thermophysics, 8 (1987) 481-510.
87. Z. Li, S. Bigdeli, H. Mao, Q. Chen, M. Selleby, Thermodynamic evaluation of pure Co for the third generation of thermodynamic databases, Physica Status Solidi (b), 254 (2017) 1600231.
88. Y. Terada, K. Ohkubo, T. Mohri, T. Suzuki, Thermal conductivity of cobalt-base alloys, Metallurgical and Materials Transactions, 34A (2003) 2026-2028.
89. M.J. Assael, K.D. Antoniadis, W.A. Wakeham, M.L. Huber, H. Fukuyama, Reference correlations for the thermal conductivity of liquid bismuth, cobalt, germanium, and silicon, Journal of Physical and Chemical Reference Data, 46 (2017) 033101.
90. A.C. Yu, T.M. Donovan, W.E. Spicer, Optical properties of cobalt, Physical Review, 167 (1968) 670-673.
91. E. Siegel, Optical reflectivity of liquid metals at their melting temperatures, Physics and Chemistry of liquids, 5 (1976) 9-27.

92. D. R. Lide (ed), CRC Handbook of Chemistry and Physics. CRC Press. Boca Raton, Florida, Internet version 2005; Section 10, Atomic, Molecular, and Optical Physics; Ionization Potentials of Atoms and Atomic Ions.
93. A. Kramida, Yu. Ralchenko, J. Reader and NIST ASD Team (2022). NIST Atomic Spectra Database (ver. 5.10), [Online]. Available: https://physics.nist.gov/asd [accessed on 2023, April 21]. National Institute of Standards and Technology, Gaithersburg, MD
94. https://www.nagwa.com/en/explainers/930186872308/ (accessed on 12/17/2023).
95. Y.F. Shen, D.D. Gu, Y.F. Pan, Balling process in selective laser sintering 316 stainless steel powder, Key Engineering Materials, 315-316 (2006) 357-360.
96. S. Schiaffino A.A. Sonin, Molten droplet deposition and solidification at low Weber numbers, Physics of Fluids, 9 (1997) 3172-87.
97. X. Liu, X. Zhang, J. Min, Spreading of droplets impacting different wettable surfaces at a Weber number close to zero, Chemical Engineering Science, 207 (2019) 495-503.
98. Y. Tatekura, M. Watanabe, K. Kobayashi, and T. Sanada, Pressure generated at the instant of impact between a liquid droplet and solid surface, Royal Society open science, 5 (2018) 181101.
99. R. Fabbro, J. Fournier, P. Ballard, D. Devaux, J. Virmont, Physical study of laser-produced plasma in confined geometry, Journal of Applied Physics, 68 (1990) 775-84.
100. Meyers MA. Dynamic Behavior of Materials. John Wiley & Sons, 1994.
101. S. Blairs, Sound velocity of liquid metals and metalloids at the melting temperature, Physics and Chemistry of Liquids, 45 (2007) 399-407.
102. B.J. Keene, Review of data for the surface tension of pure metals, International Materials Reviews, 38 (1993) 157-192.
103. H. Hess, E. Kaschnitz, G. Pottlacher, Thermophysical properties of liquid cobalt, International Journal of High Pressure Research, 12 (1994) 29-42.
104. https://www.tec-science.com/thermodynamics/kinetic-theory-of-gases/mean-free-path-collision-frequency/ (accessed on 12/17/2023).
105. A.V. Phelps, C. H. Greene and J. P. Burke Jr. "Collision cross sections for argon atoms with argon atoms for energies from 0.01 eV to 10 keV." Journal of Physics B: Atomic, Molecular and Optical Physics, 33 (2000) 2965.
106. V. Aslanyan and G. J. Tallents, Local thermodynamic equilibrium in rapidly heated high energy density plasmas, Physics of Plasmas, 21 (2014) 062702.

Supplemental Material

This document contains some supplemental material for this paper, which is given here to avoid making the main body of the paper excessively long. The references cited in this document are given in the list of references for the main body of the paper.

1. Some Additional Information about the Model

1.1 The "Powder Bed Module in the Sintering Pulse Stage"

The computational domain of this module is the region with r = 0 to 160 μm and z = 0 to ~(-220) μm. The r-diction mesh size is uniform with Δr = 0.5 μm. The z-direction mesh size is non-uniform with the minimum Δz = 138 nm at the powder bed surface. The value of Δz becomes larger with a constant expansion ratio of 1.05 as it goes from z = 0 to z = ~(-220) μm. It is assumed that the powder bed's initial temperature is uniform and equal to 300 K at t = 0.

Based on the model-calculated peak temperature of the powder bed surface during the entire sintering pulse stage (t = 0 to 365 μs) and the Hertz-Knudsen equation [7, 44, 51-53], a peak surface evaporation velocity is obtained. Assuming the peak evaporation velocity for the entire sintering pulse stage, the thickness of evaporated powder bed material is less than ~0.2 nm. This is a negligibly small value. Hence, although the evaporation-induced energy loss from the surface is considered in solving Eq.(2), the induced mass exchange between the powder bed and the ambient gas phase (as well as the energy carried by the vapor into the ambient gas) is neglected in the sintering pulse stage.

A simulation with the module was performed by adding the surface heat loss due to thermal radiation: $\sigma(T_s^4 - T_a^4)$, where T_a represents the ambient temperature assumed to be 300 K and σ denotes the Stefan–Boltzmann constant. The emissivity is assumed to be 1 to get the upper limit

of the heat loss. The mode-predicted peak temperatures of the powder bed surface during the entire sintering pulse stage with and without considering the thermal radiation differ by less than ~0.02 K. Hence, the surface heat loss due to thermal radiation is neglected in this module.

The powder-air heat transfer (including the convection heat loss of the powder bed surface to the air) is expected to have a small effect on the powder temperature history because cobalt has a much larger heat capacity per unit volume than air. At 1 atm and the room temperature, the cobalt-air volumetric heat capacity ratio is on the order of ~3200:1 [16, 33, 68-70]. At t = 365 μs (the end of the sintering pulse stage), in the entire computational domain the increase of the total internal energy of the air compared with the air at t = 0 can be called ΔE_{air}, which is mainly due to the powder-air heat transfer (the kinetic energy of air is negligibly small compared with its internal energy and hence not considered). Similarly, the increase of the total internal energy of the cobalt powder is called ΔE_{powder}. Based on the simulation result with the model, ΔE_{air} is only ~2% of ΔE_{powder}. Thus, the powder-air heat transfer is expected to have a small overall effect on the powder temperature history and is neglected in the calculation in the "Powder Bed Module in the Sintering Pulse Stage".

1.2 The "Air Module in the Sintering Pulse Stage"

As shown in the authors' previous experimental study in Ref. [13], the sintered material using only the ~200-ns sintering pulses is still highly porous. Hence, in the "Powder Bed Module in the Sintering Pulse Stage", similar to the authors' previous paper [7], it is assumed that upon powder full melting the porosity changes from its initial value $\varepsilon_{p,s}$ to a new value $\varepsilon_{p,l}$, such that the effective density of the powder-bed medium remains the same, i.e., $\rho_s(1-\varepsilon_{p,s}) = \rho_l(1-\varepsilon_{p,l})$, where ρ_s and ρ_l are the bulk densities of the solid and liquid cobalt, respectively. Because ρ_s and ρ_l are reasonably close [16], $\varepsilon_{p,s}$ and $\varepsilon_{p,l}$ are close, too. In the "Air Module in the

Sintering Pulse Stage", as a reasonable simplification, a constant porosity of 0.69 is used in solving the continuity and momentum equations for the air flow in the porous powder bed medium. As detailed in the authors' previous paper [7], to account for the initial solid particle agglomeration, an effective particle diameter of 2.56 μm has been used in both the "Powder Bed Module in the Sintering Pulse Stage" and the "Air Module in the Sintering Pulse Stage".

In Eq.(3b) of the paper (i.e., the momentum equation for the air in the pores of the powder bed), $\vec{F}_d$ is the volumetric force on the air due to the powder particles, given by [66]:

$$\vec{F}_d = -\varepsilon_p \frac{\mu}{K_p} \vec{u} \qquad \text{(s.1)}$$

except that the component of $\vec{F}_d$ in z direction, F_z, is given by:

$$F_z = -\varepsilon_p \frac{\mu}{K_p} u_z, \quad \text{if} \quad u_z \leq 0 \qquad \text{(s.2.1)}$$

$$F_z = -minimum \left[\varepsilon_p \frac{\mu}{K_p} u_z, \rho_{co} g \left(1 - \varepsilon_p\right) \right], \text{if} \quad u_z > 0 \qquad \text{(s.2.2)}$$

where μ is the air viscosity, ρ_{co} is the bulk cobalt density, g is the gravitational acceleration, and K_p is the permeability given by [66]:

$$K_p = \frac{d^2}{180} \frac{\varepsilon_p^3}{(1-\varepsilon_p)^2} \qquad \text{(s.2.3)}$$

where d is the average powder particle diameter. For Eq. (s.2.2), it has been roughly assumed that the maximum force exerted by the powder particle on the air in the –z direction does not exceed the gravity force of the powder.

In the "Air Module in the Sintering Pulse Stage", the mass, momentum and energy conservation equations are solved for the *ambient air region* above the powder bed surface. The mass and momentum equations solved are the same as Eqs.(3a) and (3b), except that the porosity is 1. The energy conservation equation is given by [70, 74]:

$$\frac{\partial \rho h}{\partial t} - \frac{\partial P}{\partial t} + \nabla \cdot (\rho h \vec{v}) = \nabla \cdot (k \nabla \mathrm{T}) + \rho \vec{g} \cdot \vec{v} + \nabla \cdot (\bar{\tau} \cdot \vec{v}) \qquad \text{(s.3)}$$

where h is the air enthalpy per unit mass, T denotes the temperature, and k represents the thermal conductivity.

In the energy equation, the air kinetic energy per unit volume is neglected because it is typically much smaller than the air internal energy per unit volume under the studied condition. Based on the simulation result with the "Air Module in the Sintering Pulse Stage", at t = 365 μs (the end of the sintering pulse stage) most of the air (representing 98.3% of the total air mass in the entire computational domain) is at temperatures below 350 K. Hot air above 500 K and 1000 K only represents 0.18% and 0.0083% of the total air mass, respectively. The air specific heat C_p changes slowly with temperature [68], and thus in this module C_p is assumed to be constant and equal to 3.5R (i.e., 1004 J/kg·K), the value for a perfect diatomic gas, where R is the specific gas constant for air [68-70].

The computational domain of the "Air Module in the Sintering Pulse Stage" has two portions. The portion in the powder bed has the same size as the domain of the "Powder Bed Module in the Sintering Stage", while the portion above the powder bed surface is the domain within r = 0 to ~241 μm and z = 0 to ~561 μm in the radial and axial directions, respectively. In the powder-bed portion of the domain, the z-direction mesh size (Δz) is ~0.281 μm near the powder bed surface at z = 0. As the mesh location goes away from the surface, the mesh size gradually expands with a size ratio of ~1.145 between adjacent mesh cells. The r-direction mesh size (Δr) is ~1.346 μm near r = 0 and expands with r with a size ratio of ~1.0826. In the domain portion above the powder bed, Δz is ~0.289 μm near z = 0 and expands with z with a ratio of ~1.1142. The size of Δr is the same as that for the powder-bed domain in the range of r = 0 to 160 μm, while Δr = ~16.225 μm in the range of r = 160 to ~241 μm.

The governing equations are solved numerically using a modified buoyantPimpleFoam solver based on the PIMPLE algorithm in OpenFOAM [56, 59]. The discretization of convection terms is via the 2nd-order linear-limited scheme and diffusion terms via the 2nd-order central difference scheme while the time advancement is achieved by employing the Crank-Nicolson implicit method [55, 56]. A variable Δt is used in the simulation such that at each numerical time step the Courant number in the computational domain does not exceed 0.1.

Simulations were performed using the "Air Module in the Sintering Pulse Stage" with the turbulent model option turned on in OpenFOAM (the $k-\omega$ *SST* and $k-\varepsilon$ turbulence models with the default turbulence model parameters given in OpenFOAM were used). The simulation results at t = 365 μs do not have any obvious difference from that without considering turbulence. For example, the curves for the temperature of air versus z at r = 0 for the region above the powder bed surface almost completely overlap with or without considering turbulence. Hence, for the result given in this paper, turbulence is not considered.

1.3 The "Pressing Pulse Stage Module"

In this module, the thermal conductivity of the powder bed medium used is determined in a way similar to that for the "Powder Bed Module in the Sintering Pulse Stage". One exception is that for the powder bed surface layer within the depth equal to the particle effective diameter, the *z*-direction (i.e., the depth-direction) conductivity is assumed to be the same as that for the bulk cobalt. This is because the pressing laser pulse has a very short duration and can cause a very high temperature gradient in a very thin surface layer (with a thickness smaller than the particle effective diameter d_p). The heat conduction in z direction within such a thin layer is expected to be similar to that in the bulk cobalt because the inter-particle boundary is not involved yet. In this case, it is

expected to be more accurate to use the bulk cobalt thermal conductivity to calculate the z-direction heat conduction in the surface layer within the depth of d_p.

The equation of state (EOS) table for the ionized cobalt vapor is established by solving the Saha equation to get free electron and ion number densities (and then the pressure as well as internal energy per unit volume) for each T-ρ pair in the EOS table [69, 75]. For the other gaseous region, the ideal gas EOS is utilized in the model calculation. The possible laser beam absorption (the last term on Eq.(4e)'s right side) by the gaseous material is assumed to be mainly due to the electron-ion inverse bremsstrahlung process and calculated accordingly based on the gas temperature, free electron and ion densities [76]. The thermal conductivity in the vapor region is calculated based on the vapor free electron density and temperature [77].

For this module, the numerical solution procedure is similar to that in Ref. [44]. Once surface evaporation starts, in each numerical time step, the solution of the heat transfer equation provides the updated powder-bed surface temperature T_{suf}, based on which the corresponding saturation vapor pressure P_s at this temperature can be calculated using the Clausius–Clapeyron equation [44, 52]. The solution of the gas dynamic equations provides the pressure P right above the Knudsen layer (KL). Based on the pressure ratio P/P_s and the KL relations [44, 51, 52, 72, 81-84], the vapor temperature, density and z-direction velocity right above the KL can be determined, from which the evaporation flux can be calculated. Based on the evaporation flux the vaporization velocity V_{vap} for the heat transfer equation of the powder bed is calculated. Then, the same procedure repeats for the next time step. The gas dynamic equations are solved numerically using the explicit ENO method [85].

A uniform mesh is used in the gaseous phase region with $\Delta r = \Delta z = 0.5$ μm. The computational domain for the gaseous phase in the "Pressing Pulse Stage Module" is the region

with r = 0 to 160 μm and z = 0 to 310 μm. The computational domain for the powder bed is the region with r = 0 to 160 μm and z = 0 to ~(-215) μm. A uniform mesh size is used in the r-direction with Δr = 0.5 μm. The mesh size in the z direction has the smallest value at the powder bed surface (Δz = 30 nm), and then increases with a constant ratio of 1.1 between neighboring numerical cells as it goes from the powder bed surface to the domain bottom boundary.

2. Justification of the Use of One-temperature Gas Dynamic Equations in the "Pressing Pulse Stage Module"

The internal energy of the ionized cobalt vapor includes: (i) the kinetic energy of heavy particles (atoms and ions), (ii) the kinetic energy of free electrons, and (iii) the potential energy related to the generation of the free electrons (i.e., the ionization of neutral particles) [69]. In the Equation of State (EOS) utilized for cobalt in the model, all the three energy components are considered.

The ionization degree of the cobalt vapor modeled in this study is typically very low. It has been found that if the cobalt vapor ionization is neglected and only the ideal gas EOS is used (i.e., only the heavy particles' kinetic energy is considered in the internal energy), the simulation result in the "Pressing Pulse Stage Module" for the plasma plume evolution does not change very significantly for the conditions studied. For example, compared with the simulation result neglecting the cobalt vapor ionization, in the simulation result considering the cobalt vapor ionization: (1) the temporally peak total pressure exerted on the powder bed surface at r = 0 differs by less than 0.1%; (2) the gas temperature distribution along z at r = 0 and t = 6 ns is very close, except a very thin layer of less than ~1 μm around the peak temperature location, where the peak temperature differs by ~26%; and (3) the gas temperature distribution along z at r = 0 and t = 10

ns is very close for the entire gas domain. That means overall the kinetic energy of heavy particles dominates over the other energy components (ii) to (iii), and the evolution of heavy particles plays the major role in the plasma evolution in this study.

Therefore, regardless of whether or not the electrons and heavy particles have the same temperature, the one-temperature gas dynamic equations used in the model can provide a reasonably good description of the gas dynamic process as long as the kinetic energies of the heavy particles follow a Maxwell velocity distribution [69, 77] such that their temperatures can be meaningfully defined. Whether or not this condition is satisfied can be checked based on the neutral particle collision time (i.e., the duration between successive neutral particle collisions) τ_{nn}, which can be estimated as [104]:

$$\tau_{nn} = \frac{1}{\sqrt{2} n_a \sigma V_{th}} \qquad \text{(s.4)}$$

where n_a is the number density of neutral atoms or molecules, σ is the collision cross section (although the authors did not find an exact value for the cobalt atom, σ for many atoms is often on the order of 10^{-15} to 10^{-14} cm^2 [77, 104, 105]. The value of 10^{-15} cm^2 is used to estimate a relatively large value for τ_{nn}.), and V_{th} is the mean thermal speed [104]:

$$V_{th} = \sqrt{\frac{8 k_b T}{\pi m}} \qquad \text{(s.5)}$$

Where T is temperature, m is the mass of the atom or molecule and k_b is the Boltzmann constant. Based on the calculations using the model and Eqs. (s.4) and (s.5), at t = 35 ns, 55 ns and 75, τ_{nn} for most spatial points within the plume is typically smaller than ~1 ns, a few ns and 10 ns, respectively. Therefore, for the simulated time range, τ_{nn} for most spatial points in the plume (where the plume front is defined as the temperature-jump location) is typically much smaller than the simulated time scale. If neutral-ion and ion-ion collisions are also considered, then the overall

collisional time among heavy particles will be even shorter. Hence, overall the temperature of heavy particles can be reasonably meaningfully defined and the gas dynamic equations solved in the "Pressing Pulse Stage Module" is expected to provide a reasonably good description of the gas dynamic process. The model-predicted temperatures can reasonably reflect the heavy particles' temperature T_p.

3. Additional Information about the Model-Experiment Comparison on Temperature

Figure 8 of the paper shows the model-predicted plasma temperature evolution with time, in comparison with the experimentally deduced temperature. In the OES measurement, the ICCD gate is open from t = 35 to 75 ns, represented by the time error bar in Fig.8. In the experiment, it is expected that the optical emission is collected from the entire plasma region, and thus the deduced temperature is for the cobalt vapor in the whole plasma plume. It can be very roughly understood as the weighted spatially average temperature of the plasma, with the weight being the plasma optical emission intensity at each spatial point (r, z) for the spectral lines utilized in the Boltzmann plot to deduce the temperature. Under the optically thin and local thermodynamic equilibrium (LTE) assumption, the optical emission intensity for the six spectral line peaks used in the Boltzmann plot is approximately proportional to $n_a(r,z)\sum_{m=1}^{6} g_m A_{mn} e^{-E_m/(k_b T(r,z))}/\lambda_{mn}$ [34, 35], where $T(r,z)$ and $n_a(r,z)$ are the temperature and the cobalt neutral atom number density at (r, z), respectively, g_m and E_m are the upper level's statistical weight and energy for each of the six spectral lines used in the Boltzmann plot, λ_{mn} is the photon wavelength for the m-n transition, and A_{mn} is the corresponding transition probability. To make the model-experiment comparison meaningful, in Fig.8 the model-predicted plasma temperature plotted is the weighted spatial average of the model-predicted cobalt vapor temperature with the weight at each spatial point equal to $n_a(r,z)\sum_{m=1}^{6} g_m A_{mn} e^{-E_m/(k_b T(r,z))}/\lambda_{mn}$.

In Fig. 8 of the paper, the measured *excitation* temperature of cobalt neural atoms in the plasma, T_{exc}, is deduced from the OES signal measured with the ICCD gate opening from t = 35 ns to 75 ns. It can be roughly treated as the average excitation temperature in the 40 ns period from t = 35 ns to 75s. In Fig.8, the excitation temperature T_{exc} is compared with the model-predicted temperature (which is close to T_p as introduced in Section 2 of this document). Next, it will be shown that the comparison of the measured T_{exc} with the model-predicted T_p, although very approximately, is still meaningful.

The time scale τ_{ep} for the energy exchange between electrons and cobalt heavy particles (cobalt atoms and ions) can be estimated based on the following relation [69]:

$$\frac{1}{\tau_{ep}} = \frac{1}{\tau_{ei}} + \frac{1}{\tau_{ea}} \qquad \text{(s.6)}$$

where τ_{ei} and τ_{ea} are the electron-ion and electron-neutral atom energy relaxation time given by [69, 77]:

$$\tau_{ei} = 3.5 \times 10^8 A T_{ev}^{1.5} \Big/ \left[n_i z^2 ln\left(\frac{12\pi}{ze^3} \sqrt{\frac{\varepsilon_0^3 k_b^3 T^3}{n_e}} \right) \right] \qquad \text{(s.7)}$$

$$\tau_{ea} = \frac{m}{2 n_a V_e \sigma_{elast} m_e} \qquad \text{(s.8)}$$

where A is the ion's atomic weight, T_{ev} is the electron temperature in the unit of eV, T is the electron temperature in the unit of K, n_i denotes the ion number density (cm^{-3}), z is the ion charge number, e is the electron charge, ε_0 is the vacuum permittivity, k_b is the Boltzmann constant, n_e is the electron number density (m^{-3}), m and m_e are the atom and electron masses, respectively, n_a denotes the neutral atom number density (m^{-3}), V_e is the electron average thermal speed, and σ_{elast} is the cross section for the electron-neutral atom elastic collision. In this study, the plasma ionization degree from the simulation is very low and Co^+ is the dominant type of ions in the vapor. Hence, it can be approximately assumed that $z = 1$ and $n_i = n_e$. The authors did not find the exact

value of σ_{elast} for cobalt, but σ_{elast} is often on the order of ~10^{-15} to 10^{-14} cm^2 in metals [77] (10^{-15} cm^2 is used in the calculation below to estimate a relatively large value for τ_{ea}). The electron average thermal speed is given by [69]:

$$V_e = \sqrt{\frac{8k_bT}{\pi m_e}} \qquad \text{(s.9)}$$

Using the model-predicted spatially average temperature and electron density for cobalt vapor as well as the neutral cobalt atom density deduced from EOS based on the temperature and electron density, from Eqs. (s.6) to (s.9), the value of τ_{ep} is estimated to be ~12 ns, ~23 ns and ~38 ns at t = 35, 55 and 75 ns, respectively. In the calculation, at each moment the model-predicted vapor temperature in Fig.8 (which is the weighted average in space as introduced earlier in this document) is used for the electron temperature in Eqs.(s.7) and (s.9), while the model-predicted free electron density (averaged in space in a way similar to that for the temperature) is used for the electron density in Eq. (s.7).

It can be seen that τ_{ep} is still smaller than the 40 ns gate width of the ICCD for the OES measurement in the time range of t = 35 to 75 ns. Hence, the temporally averaged temperatures of electrons and heavy particles for the 40-ns period from t = 35 to 75 ns should be reasonably close ($T_e \approx T_p$).

Using the model-predicted temperature and free electron density for cobalt vapor (the weighted average values in space as introduced earlier) and the spectroscopic data given in Table 1 of the paper, the following McWhirter's criterion [34, 37, 38] is found to be satisfied for t = 35 to 75 ns:

$$n_e \geq 1.6 \times 10^{12} T^{0.5} (\Delta E)^3 \qquad \text{(s.10)}$$

where n_e is the free electron number density in the unit of cm^{-3}, T denotes the temperature in the unit of K, and ΔE denotes the largest energy transition involved (in the unit of eV). The satisfaction

of the McWhirter's criterion provides supporting evidence that the collisional excitation process for cobalt neutral atoms dominates over the radiative de-excitation process [106] for the energy levels listed in Table 1. The collisional excitation process for cobalt neutral atoms involves collisions of the atoms with electrons and/or heavy particles. It has been shown earlier that $T_e \approx T_p$ for the average temperature from t = 35 to 75 ns. Therefore, the average excitation temperature of the cobalt atoms in this period deduced from OES is likely to be reasonably close to the temperatures of electrons and heavy particles, i.e., $T_{exc} \approx T_e \approx T_p$. Therefore, the comparison of the measured T_{exc} with the model-predicted T_p in Fig.8 of the paper is meaningful.

4. Further Discussions on Some Simplified Assumptions in the Model

The model in this paper is based on some simplifications intended to get an affordable computational cost. There is certainly room to improve the model by removing the simplifications, but such an improvement might also cause a very high or even unacceptable computational cost.

For example, the molten metal flow in the powder bed has not been considered in the model. The model simulated the plasma evolution induced by one laser pulse group comprising 10 "sintering laser pulses" followed by 1 "pressing laser pulse". The entire simulated duration is not very long (< 366 μs). It is expected that the melt flow during such a short period will not significantly affect the simulated plasma evolution. The plasma is generated by the ~4-ns pressing laser pulse and the plasma evolution well within 100 ns of its generation is simulated. The effect of melt flow within the 100 ns is expected to be small. The ten ~200-ns sintering pulses before the pressing pulse span a longer duration, but their effects on the plasma are indirect and less significant than the pressing pulse. Neglecting melt flow is a limit of the model. It will improve the model if the melt flow is considered. However, that might involve the simulation of the flow

of numerous small melted particles (droplets) and an extremely high (or even unaffordable) computational cost due to the very small size and thus large number of the particles involved in this study.

In the "Powder Bed Module in the Sintering Pulse Stage" of the model, the absorption of the ten ~200-ns sintering pulses in the powder bed is calculated using the analytical model from Ref. [50], which was developed based on the radiation transfer equation (RTE) considering the scattering (including multiple reflections) effect based on geometrical optics. Ref. [50] shows that the prediction from the analytical model can agree reasonably well with a ray tracing simulation for a powder bed with a thickness of several hundred micrometers. The analytical model in Ref. [50] did not consider the diffraction effect. As mentioned in Ref. [50], the geometrical optics approximation is applicable when $\pi D_p \geq 5\lambda$, where D_p is the particle diameter and λ denotes the laser wavelength. This condition is satisfied in this study according to the utilized laser wavelength and the effective particle diameter (the latter is given in Section 1.2 of this document).

In the "Powder Bed Module in the Sintering Pulse Stage" of the model, for solid powder that has not melted yet it is roughly assumed that the effective thermal conductivity k_{eff} is 3% of the bulk cobalt conductivity k_{co}. The value of 3% is estimated based on the information in Ref. [46], which reports a computational modeling study of metal powder thermal conductivity. When the medium is in the molten state (or re-solidified after melting), it is assumed $k_{eff} = k_{co}(1-\varphi) + k_{air}\varphi$ [49], where k_{air} is the air thermal conductivity. The melted powder conductivity calculated in this way is much larger than 3% of the bulk metal conductivity. Hence, the model has considered the increase of the effective conductivity of the powder material upon melting. The model will be improved if the continuous variation of the thermal conductivity as the particle coalition proceeds can be considered based on the dependence of the conductivity on the

sintering level. However, this might require the simulation of the evolution of individual particles, which could be computationally too expensive due to the small particle size and the large particle number involved.

It should be noted that in the authors' previous paper [7], the temperature evolution of a cobalt powder bed (with the same particle size as that in this paper) induced by ten ~200-ns laser pulses with a 40-μs inter-pulse separation was simulated by solving the heat transfer equation assuming the powder bed is a continuum medium. The model has simplifications similar to that in the "Powder Bed Module in the Sintering Pulse Stage" in this paper: it neglects the melt flow, uses the analytical model in Ref. [50] to simulate laser beam propagation and energy absorption in the powder bed, and assumes that the effective thermal conductivity of the solid powder bed medium is 3% of the bulk metal conductivity. The powder bed surface temperature predicted by the model in Ref. [7] shows an acceptable agreement with the measured temperature under the condition studied in Ref. [7]. The agreement provides supporting evidence that the aforementioned simplifications, although approximate, can still provide acceptable accuracy.

5. Some Other Related Information

In Fig.7 of the paper, the model-predicted plasma top front is assumed to be the temperature jump front in the gaseous phase at r = 0 from the simulation, while the measured plasma front is the visible top boundary of the plume shown in the ICCD image.

The laser-induced radiation pressure exerted on perfectly absorbing and reflective surfaces are given by I/c and $2I/c$ [94], respectively, where I is the laser intensity and c is speed of light. For $I = 1\ GW/cm^2$, the radiation pressure for a perfectly reflective surface is only ~0.67 atm. In

this study, laser intensity is much smaller than 1 GW/cm^2 and thus the radiation pressure is insignificant and not considered in calculating the total pressure exerted on the powder bed surface.

Typically, it is expected that solid crack formation due to the plasma-induced mechanical pressure should not be a big issue for DP-LMS of metal powders. In our previous studies reported in Refs. [12, 13, 15], we were not aware of obvious solid crack formation in the sintered material due to plasma-induced mechanical pressure under the studied conditions for DP-LMS with suitable parameters. Typically, when the pressing laser pulse arrives, the laser spot center on the powder bed surface is melted material. At a certain location away from the spot center on the powder bed surface, the material changes from melt to solid, but the plasma-induced pressure is also lower than the peak pressure at the spot center (see Fig.11 of the paper). "If" in a certain situation, the plasma-induced mechanical pressure causes cracks in the solid region, then it is still possible to reduce the pressing laser pulse intensity, such that the plasma-induced pressure is high enough to promote melt flow (to reduce balling and enhance densification for the re-solidified material) and meanwhile low enough to avoid cracks in the solid region surrounding the melt pool. Such a laser intensity is expected to exist because typically the pressure needed to promote melt flow should be lower than the pressure generating cracks in the surrounding solid region.

Based on images taken by a camera, some random material spattering (which is likely associated with powder denudation) from the powder bed was ever observed for both the DP-LMS process and the sintering process using only the "sintering laser pulses".

This study has revealed the effect of the "sintering pulses" on the "pressing pulse"-induced plasma from *a powder bed* in DP-LMS. The studied situation is very different from the previous studies in Ref. [30-32] for multi-pulse laser-induced plasma and/or laser-plasma interactions for *air or a bulk metal target*. In this study, the "sintering pulses" do not generate a plasma plume and

do not induce obvious ablation or surface evaporation, and thus the "pressing pulse" does not interact with a pre-existing plasma plume. In the studies in Refs. [30-32], each laser pulse participates in the generation of a plasma plume and/or interacts with a pre-existing plume induced by previous laser pulse(s).